



Novel quadratic Bézier triangular and tetrahedral elements using existing mesh generators: Applications to linear nearly incompressible elastostatics and implicit and explicit elastodynamics

C. Kadapa

Swansea Academy of Advanced Computing, Swansea University, Singleton Campus, Swansea SA2 8PP, Wales, UK.

SUMMARY

In this paper, we present novel techniques of using quadratic Bézier triangular and tetrahedral elements for elastostatic and implicit/explicit elastodynamic simulations involving nearly incompressible linear elastic materials. A simple linear mapping is proposed for developing finite element meshes with quadratic Bézier triangular/tetrahedral elements from the corresponding quadratic Lagrange elements that can be easily generated using the existing mesh generators. Numerical issues arising in the case of nearly incompressible materials are addressed using the consistent **B**-bar formulation, thus reducing the finite element formulation to the one consisting only of displacements. The higher-order spatial discretisation and the non-negative nature of Bernstein polynomials are shown to yield significant computational benefits. The optimal spatial convergence of the **B**-bar formulation for the quadratic triangular and tetrahedral elements is demonstrated by computing error norms in displacement and stresses. The applicability and computational efficiency of the proposed elements for elastodynamic simulations are demonstrated by studying several numerical examples involving real-world geometries with complex features. Numerical results obtained with the standard linear triangular and tetrahedral elements are also presented for comparison. Copyright © 0000 John Wiley & Sons, Ltd.

Received ...

KEY WORDS: Bézier elements; Bernstein polynomials; Explicit elastodynamics; B-bar formulation; Connecting rod

*Correspondence to: E-mail: c.kadapa@swansea.ac.uk

This article has been accepted for publication and undergone full peer review but has not been through the copyediting, typesetting, pagination and proofreading process, which may lead to differences between this version and the Version of Record. Please cite this article as doi: 10.1002/nme.5967

1. INTRODUCTION

The increasing need for optimised designs in commercial and industrial applications requires efficient and cost-effective numerical techniques for the simulations of problems involving complex geometries and intricate shapes. In such cases, numerical techniques based on finite element discretisations that can be created using existing mesh generators always attract the interest of simulation engineers.

Of all the numerous types of polynomial spaces used for finite element discretisations those based on the Lagrange polynomials are well-established and are widely used in the field of computational mechanics. Among the Lagrange family of finite elements, triangular/tetrahedral elements are often the favourable choice because of the ease of mesh generation, even for complicated industrial geometries, and the availability of numerous commercial and open-source mesh generation software suites. In the past few decades, a plethora of numerical techniques have been developed for performing simulations using triangular and tetrahedral elements, as the task of mesh generation with triangular and tetrahedral elements is well established.

Nevertheless, in spite of the tremendous amount of research work that has gone into the development of numerical techniques for obtaining accurate numerical solutions using triangular/tetrahedral elements, robust and efficient techniques for performing simulations using these elements are still lacking, especially for explicit elastodynamic simulations involving nearly incompressible material models which are commonly encountered in soils, a majority of polymeric materials and biological tissues. This lack of development is owing to the fact that triangular/tetrahedral Lagrange elements suffer from quite a few disadvantages that limit their applicability to explicit elastodynamic simulations consisting of nearly incompressible elastic and elastoplastic material models. The important disadvantages of triangular/tetrahedral Lagrange elements that motivated the present research work are:

- Due to the approximation of constant strain across the element, linear triangular/tetrahedral Lagrange elements with pure displacement formulation exhibit very stiff behaviour when compared with the linear quadrilateral/hexahedral Lagrange elements [1]. Therefore, to obtain numerical results of sufficient accuracy, even for compressible materials, the finite element meshes with linear triangular/tetrahedral elements have to be significantly finer than the corresponding quadrilateral/hexahedral meshes; thus, negating the benefits of ease of mesh generation. Moreover, for nearly incompressible elastic and elastoplastic material models, linear triangular/tetrahedral elements are known to perform the poorest among the well-established finite elements.
- Even though accurate numerical results can be obtained with coarse meshes using higher-order Lagrange triangular/tetrahedral elements, their main disadvantage is that they are not directly amenable for explicit dynamic simulations due to the presence of negative entries in the mass matrix which result in zero-diagonal entries for the standard lumped-mass matrices. Furthermore, non-uniform contributions from the edge/surface loads to the edge/surface nodes pose numerical issues in contact-impact modelling using higher-order Lagrange elements.

Numerous sophisticated formulations have been proposed over the past couple of decades to obtain meaningful numerical results by overcoming the disadvantages discussed above. A majority of the schemes proposed to address the issues with triangular/tetrahedral elements for modelling nearly and fully incompressible materials involve sophisticated modifications and complex implementations, and many of these techniques are often limited to static analyses while some only to transient problems. The amount of literature on numerical methods for modelling nearly incompressible materials using triangular and tetrahedral elements is quite exhaustive. In this work, we discuss only some important contributions and refer the reader to the references therein for the details on other such techniques.

Some of the noteworthy contributions for modelling nearly incompressible materials using triangular and tetrahedral elements include: averaged nodal pressure approach by Bonet et al. [2], fractional-step based projection schemes by Zienkiewicz, Pastor and collaborators [3, 4], node-based uniform strain elements by Dohrmann et al. [5], mixed-enhanced formulation by Taylor [6], composite triangular element by Guo et al. [7], composite tetrahedral element by Thouthireddy et al. [8], stabilised nodally integrated elements by Puso and Solberg [9], smoothed finite element method by Liu et al. [10, 11], assumed-deformation gradient methods by Brocardo et al. [12], F-bar patch for triangular and tetrahedral elements by de Souza Neto et al. [13] and non-confirming tetrahedral element by Hansbo [14, 15]. To address the issues with higher-order Lagrange tetrahedral elements, Danielson [16] proposed a 15-noded tetrahedral element and Krysl et al. [17, 18] proposed 10-noded tetrahedral element with energy-sampling stabilisation.

Parallel to the above developments, in the past few decades, several researchers extended mixed-stabilised formulations to solid mechanics problems in order to model nearly incompressible materials successfully using triangular and tetrahedral elements. To the author's knowledge, the original idea of extending stabilised formulations to nearly incompressible elasticity problems was first proposed by Franca et al. [19]. Later, Maniatty and collaborators [20, 21, 22] extended this idea to nearly incompressible hyperelastic and elastoplastic material models; and Masud and Xia [23, 24] proposed multiscale/stabilised formulation for nearly incompressible elasticity and finite deformation elastoplasticity. On the similar lines, Chiumenti and Cervera group [25, 26] addressed the issues with modelling nearly incompressible materials by employing the stabilisation based on orthogonal sub-grid scales. Recently, Cervera et al. [27, 28, 29] proposed stabilised mixed displacement-stress and displacement-strain formulations for problems in elasticity.

At this point, it is important to point out that all the stabilised formulations discussed so far are limited to static problems. Even though the mixed-stabilised formulations have been successful in addressing some of the issues with modelling nearly incompressible materials, they are not wholly adequate in addressing all the issues, especially those associated with explicit elastodynamic simulations. As the time derivative of pressure is absent in the governing equations, mixed displacement-pressure formulations applied to the standard governing equations fail when used in conjunction with explicit time integration schemes. To overcome this problem, Scovazzi et al. [30, 31] proposed mixed-stabilised formulations using the rate form of the incompressibility constraint equation and successfully performed explicit elastodynamic simulations using stabilised mixed formulations. In parallel, Bonet, Gil and co-workers [34, 35, 36, 37] proposed several mixed stabilised formulations based on first-order conservation laws for performing explicit elastodynamic

simulations using the linear triangular and tetrahedral elements for problems involving nearly and truly incompressible materials.

In spite of the great success by Scovazzi et al. [30, 31, 32, 33] and Bonet, Gil and co-workers [34, 35, 36, 37] in performing explicit elastodynamic simulation using mixed-stabilised formulations, we find that these stabilised formulations are still lacking certain features that limit their applicability to general large-scale problems. Some important disadvantages of the stabilised mixed formulations are:

1. Ad-hoc stabilisation parameters that control the stability of the numerical schemes and the accuracy of numerical results are inherent to stabilised formulations. Though closed-form expressions for computing these stabilisation parameters are available, it is always preferable to avoid formulations with such mesh-size-dependent and time-step-dependent parameters.
2. It is not straightforward to account for stress discontinuities across material interfaces using formulations in which stress or hydrostatic pressure is approximated as a continuous nodal variable. Stress discontinuities across material interfaces need to be modelled with weak enforcement of interface conditions, as shown in [33].

Moreover, the behaviour of the existing stabilised mixed displacement-pressure formulations when applied to pressure-dependent constitutive models is yet to be investigated. Furthermore, owing to the inherent disadvantages of the standard higher-order Lagrange triangular/tetrahedral elements for explicit elastodynamic simulations, the mixed-stabilised formulations cannot be extended to these elements.

Coming to the paradigm of isogeometric analysis (IGA), as the polynomial spaces used in IGA are all non-negative, the resulting lumped-mass matrices suit well for explicit elastodynamics, see [38] and references therein for the comprehensive discussion on IGA. Even though IGA offers a promising numerical framework for explicit elastodynamic simulations, it is still in its early stages. The amount of published research focussing on explicit elastodynamic simulations using IGA and other related techniques is limited, see [39, 40]; and, to the knowledge of the author, such methods are non-existent for nearly incompressible material models. Besides, as the conventional IGA is based on non-uniform rational b-splines (NURBS) which are tensor-product by nature, a majority of the research work on IGA makes use of quadrilateral/hexahedral spatial discretisations. Only recently, some efforts are made to extend IGA to triangular/tetrahedral discretisations, see [41, 42, 43, 44, 45]. Nevertheless, instead of entirely discarding IGA due to its current limitations, we extract some concepts from IGA and develop novel and efficient finite element techniques for implicit and explicit elastodynamic simulations using triangular/tetrahedral meshes that can be generated using existing mesh generators.

Thus, our present work addresses many of the difficulties associated with explicit elastodynamic simulations involving nearly incompressible materials by generating quadratic Bézier triangular/tetrahedral elements using existing mesh generators and by adopting **B**-bar formulation. The resulting formulation is (i) readily amenable for explicit dynamic simulations, (ii) computationally very efficient as it does not require additional solution variables in addition to displacements, and (iii) efficient in dealing with nearly incompressible material models. It is important to point out that the proposed scheme is applicable only to quadratic and higher-order

Bézier elements. The present work is limited to linear isotropic materials. For anisotropic materials, modifications to the **B**-bar formulation proposed by Oberrecht et al. [46] need to be considered.

The rest of the paper is organised as follows. In Section 2 we introduce the elements, present an overview of Bernstein polynomials and discuss the generation of meshes for the proposed elements using the existing mesh generators. Sections 3 and 4 are concerned with the governing equations and finite element formulations, respectively. Implicit and explicit time integration schemes used in the present work are discussed in Section 5. Spatial convergence of the proposed elements are assessed in Section 6 and numerical examples for elastodynamic simulations are presented in Section 7. A summary of the observations made and conclusions drawn are presented in Section 8.

2. ELEMENT DESIGN, MESH GENERATION AND APPLICATION OF DIRICHLET BOUNDARY CONDITIONS

The triangular and tetrahedral elements used in this work, known as Bézier triangular and Bézier tetrahedral elements, are based on the Bernstein polynomials over triangular and tetrahedral domains. In this work, finite element meshes with Bézier triangular and Bézier tetrahedral elements are generated using the existing mesh generators by exploiting the property of the Bézier curve that its end control points are interpolatory. The following subsections provide a brief overview of the Bernstein polynomials and their essential properties that form the basis for the present work. For comprehensive details on Bernstein polynomials and other related concepts discussed in this section, we refer the reader to Piegl and Tiller [47].

2.1. Bernstein polynomials

Bernstein polynomials are the class of polynomials that form the base of geometry modelling in computer graphics and computer-aided design. B-splines and NURBS are a generalisation of Bernstein polynomials over extended domains.

For the degree n , univariate Bernstein polynomials, $B_i^n(\xi_1)$, bivariate Bernstein polynomials over a triangular domain, $B_{ij}^n(\xi_1, \xi_2)$, and trivariate Bernstein polynomials over a tetrahedral domain, $B_{ijk}^n(\xi_1, \xi_2, \xi_3)$, are given by the relations,

$$B_{ij}^n(\xi_1) = \frac{n!}{i! j!} \xi_1^i (1 - \xi_1)^j, \quad i + j = n \quad (1)$$

$$B_{ijk}^n(\xi_1, \xi_2) = \frac{n!}{i! j! k!} \xi_1^i \xi_2^j (1 - \xi_1 - \xi_2)^k, \quad i + j + k = n \quad (2)$$

$$B_{ijkl}^n(\xi_1, \xi_2, \xi_3) = \frac{n!}{i! j! k! l!} \xi_1^i \xi_2^j \xi_3^k (1 - \xi_1 - \xi_2 - \xi_3)^l, \quad i + j + k + l = n \quad (3)$$

where, ξ_1 , ξ_2 and ξ_3 are the parametric coordinates such that $0 \leq \xi_1, \xi_2, \xi_3 \leq 1$.

For $n = 0$ and $n = 1$ Bernstein polynomials are precisely the same as Lagrange polynomials, and for higher-order cases they are different. As this work is focussed only on the quadratic elements, further discussion is limited to quadratic Bernstein polynomials only.

For the quadratic case ($n = 2$), there are three univariate, six bivariate and ten trivariate Bernstein polynomials. The bivariate quadratic Bernstein polynomials over a triangular domain are given by,

$$B_{002}^2(\xi_1, \xi_2) = N_1(\xi_1, \xi_2) = (1 - \xi_1 - \xi_2)^2 \quad (4)$$

$$B_{200}^2(\xi_1, \xi_2) = N_2(\xi_1, \xi_2) = \xi_1^2 \quad (5)$$

$$B_{020}^2(\xi_1, \xi_2) = N_3(\xi_1, \xi_2) = \xi_2^2 \quad (6)$$

$$B_{101}^2(\xi_1, \xi_2) = N_4(\xi_1, \xi_2) = 2\xi_1(1 - \xi_1 - \xi_2) \quad (7)$$

$$B_{110}^2(\xi_1, \xi_2) = N_5(\xi_1, \xi_2) = 2\xi_1\xi_2 \quad (8)$$

$$B_{011}^2(\xi_1, \xi_2) = N_6(\xi_1, \xi_2) = 2\xi_2(1 - \xi_1 - \xi_2) \quad (9)$$

For the purpose of discussion in the later parts of this article, and following the standard convention of representing approximation spaces, the bivariate quadratic Bernstein polynomials are also denoted using N_i , for $i = \{1, 2, 3, 4, 5, 6\}$. This numbering corresponds to the numbering of control points shown for the triangle in Fig. 1. The shapes of quadratic Bernstein polynomials are displayed schematically in Fig. 2 in the parametric coordinate system.

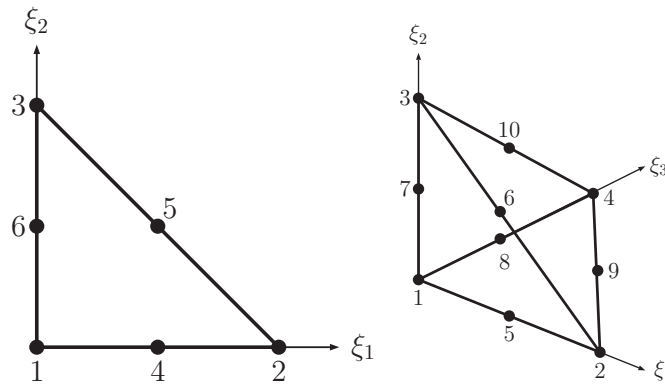


Figure 1. Quadratic triangular and tetrahedral elements in the parametric (or local) coordinates.

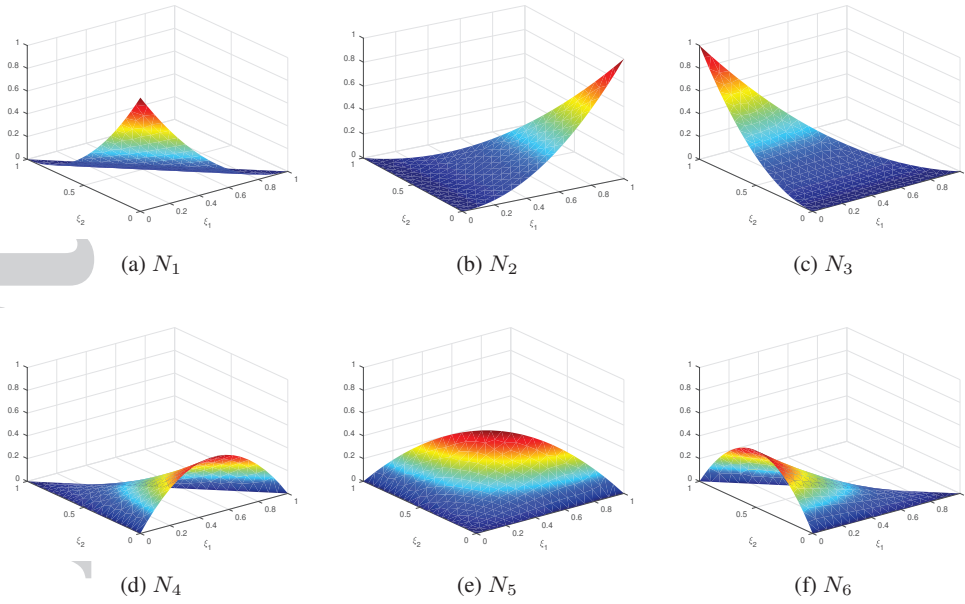


Figure 2. Quadratic Bernstein polynomials over a triangle.

2.2. Properties of Bernstein polynomials

Bernstein polynomials have the following important properties that render them suitable for finite element analysis, especially for explicit dynamic simulations:

1. Partition of unity: The sum of all the basis function is equal to unity, i.e.,

$$\sum_{i=1}^6 N_i(\xi_1, \xi_2) = 1, \quad \text{for } 0 \leq \xi_1, \xi_2 \leq 1$$

The importance of partition of unity property is that it allows to extend locally defined constructions to the whole space.

2. Non-negativity: Each Bernstein polynomial is non-negative, i.e., $N_i(\xi_1, \xi_2) \geq 0$ for $0 \leq \xi_1, \xi_2 \leq 1$; therefore, the coefficients of the mass matrix computed from the Bernstein polynomials as basis functions are all non-negative. This is the crucial property of Bernstein polynomials that renders them suitable for explicit dynamic simulations with lumped mass matrices.

2.3. Mesh generation

Mesh generation with the quadratic Bézier triangular and tetrahedral elements is based on a simple mapping technique for the mid-nodes in the Lagrange elements. This mapping technique is explained in the following paragraphs using the Bézier curve and Bézier triangle.

A Bézier curve is a parametric curve given as a linear combination of Bernstein polynomials and control points. For $n = 2$, the Bézier curve is a parabolic arc as shown in Fig. 3, and is defined as,

$$\mathbf{X}(\xi) = (1 - \xi)^2 \mathbf{P}_1 + 2\xi(1 - \xi) \mathbf{P}_2 + \xi^2 \mathbf{P}_3, \quad \text{for } 0 \leq \xi \leq 1. \quad (10)$$

where $\mathbf{P}_1, \mathbf{P}_2$ and \mathbf{P}_3 are called as control points. It can be observed from in Fig. 3 that the end control points, \mathbf{P}_1 and \mathbf{P}_3 , are interpolatory and the middle control point, \mathbf{P}_2 , is not. Using this property of the Bézier curve, quadratic Bézier elements can be generated using coordinates of the nodes, $\mathbf{X}_1, \mathbf{X}_2$ and \mathbf{X}_3 , of the quadratic Lagrange elements as follows:

- For $\xi = 0$, $\mathbf{X}(\xi = 0) = \mathbf{P}_1 = \mathbf{X}_1$
- For $\xi = 1$, $\mathbf{X}(\xi = 1) = \mathbf{P}_3 = \mathbf{X}_3$
- For any other $\xi = \hat{\xi}$ ($\hat{\xi} \neq 0$ and $\hat{\xi} \neq 1$) corresponding to node \mathbf{X}_2 ,

$$\mathbf{P}_2 = \frac{1}{2\hat{\xi}(1-\hat{\xi})} \left[\mathbf{X}_2 - (1-\hat{\xi})^2 \mathbf{X}_1 - \hat{\xi}^2 \mathbf{X}_3 \right] \quad (11)$$

When node \mathbf{X}_2 is exactly in the middle, then we have $\xi = \hat{\xi} = 0.5$, and Eq. (11) simplifies to,

$$\mathbf{P}_2 = 2 [\mathbf{X}_2 - 0.25 \mathbf{X}_1 - 0.25 \mathbf{X}_3] \quad (12)$$

which, for the special case when the nodes $\mathbf{X}_1, \mathbf{X}_2$ and \mathbf{X}_3 are collinear, i.e., for a straight line, simplifies further to, $\mathbf{P}_2 = \mathbf{X}_2$.

Using the same analogy, and assuming that the edge-nodes for the Lagrange elements are exactly in the middle, the control points for the quadratic Bézier triangular element with the numbering sequence as shown in Fig. 4 can be computed using the following relations:

$$\mathbf{P}_1 = \mathbf{X}_1 \quad (13a)$$

$$\mathbf{P}_2 = \mathbf{X}_2 \quad (13b)$$

$$\mathbf{P}_3 = \mathbf{X}_3 \quad (13c)$$

$$\mathbf{P}_4 = 2 [\mathbf{X}_4 - 0.25 \mathbf{X}_1 - 0.25 \mathbf{X}_2] \quad (13d)$$

$$\mathbf{P}_5 = 2 [\mathbf{X}_5 - 0.25 \mathbf{X}_2 - 0.25 \mathbf{X}_3] \quad (13e)$$

$$\mathbf{P}_6 = 2 [\mathbf{X}_6 - 0.25 \mathbf{X}_3 - 0.25 \mathbf{X}_1] \quad (13f)$$

Again, for the straight edges, we get, $\mathbf{P}_4 = \mathbf{X}_4$, $\mathbf{P}_5 = \mathbf{X}_5$ and $\mathbf{P}_6 = \mathbf{X}_6$.

Similarly, the control points for the quadratic Bézier tetrahedron can be computed using the nodes of the quadratic Lagrange tetrahedron element. Thus, coordinates of all the control points for the quadratic Bézier element(s) can be computed from the nodal coordinates of the quadratic Lagrange element(s) by a simple mapping technique using the relation (11) over the respective edges. In this way, finite element meshes with quadratic Bézier elements can be generated, even for complex geometries, using existing mesh generators. The computational cost of this mapping is negligible when compared with the overall theoretical and computational advantages gained, as evidenced in the later part of this article.

Remark 1: The quadratic Bézier elements considered in this work do not model exact geometry; therefore, the finite element formulation is not isogeometric. However, curved edges/surfaces can still be modelled without any difficulties using the proposed mapping technique.

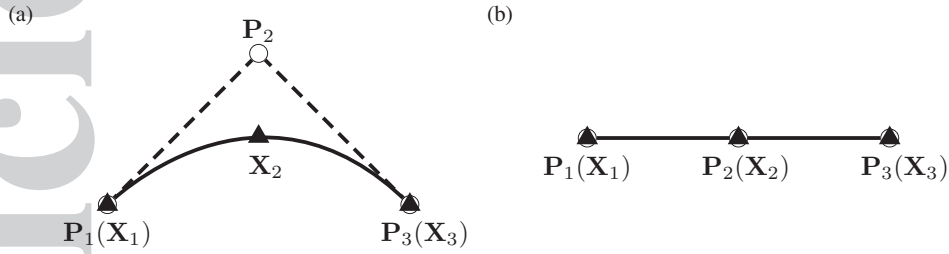


Figure 3. Quadratic Bézier curve for (a) non-collinear nodes and control points (b) collinear nodes and control points. Here \circ denotes a control point and \blacktriangle denotes a node of the Lagrange element; the dashed line represented the control polygon and the solid line represents the actual geometry of the curve.

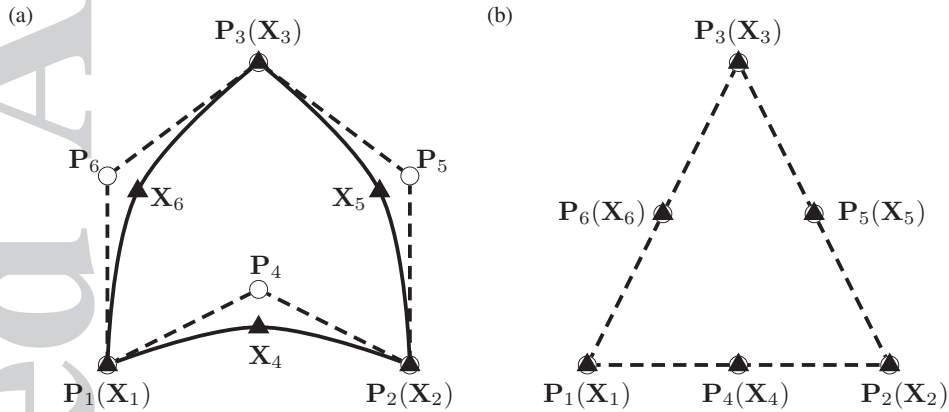


Figure 4. Quadratic Bézier triangular element with (a) curved edges and (b) straight edges. Notations are same as those in Fig. 3.

2.4. Application of boundary conditions

For the proposed elements, Neumann boundary conditions can be applied in the standard manner by evaluating the corresponding boundary integrals. However, application of Dirichlet boundary conditions seems to require special consideration since all the quadratic Bernstein polynomials are not interpolatory. While the popular Nitsche method [48] which has been adopted extensively for problems in solid and fluid mechanics [49, 50, 51] can be used for imposing the Dirichlet boundary conditions in the present work, we show that the Dirichlet boundary conditions can be applied using the standard elimination approach by extending the mapping technique for the mesh generation proposed in Section. 2.3. This mapping technique not only ensures *strong imposition of Dirichlet boundary conditions* but also eases the task of implementation of the proposed scheme into the existing finite element codes.

2.4.1. Methodology for the exact imposition of Dirichlet boundary conditions

The procedure for the imposition of Dirichlet boundary conditions is explained using the quadratic Bézier triangular element for the solution of a Laplace equation in two-dimensions. This procedure is straightforward to extend to tetrahedral elements in three dimensions as well as for problems with multiple degrees of freedom (DOFs).

Let us assume $u_1^B, u_2^B, u_3^B, u_4^B, u_5^B$ and u_6^B as the values of degrees of freedom (DOFs) at the respective control points of the quadratic Bézier triangular element shown in Fig. 4; and let us assume that $u_1^L, u_2^L, u_3^L, u_4^L, u_5^L$ and u_6^L are the corresponding DOFs values for the Lagrange element. Following the similar methodology used in deriving Eqs. (13), we get the relations,

$$u_1^B = u_1^L \quad (14a)$$

$$u_2^B = u_2^L \quad (14b)$$

$$u_3^B = u_3^L \quad (14c)$$

$$u_4^B = 2 [u_4^L - 0.25 u_1^L - 0.25 u_2^L] \quad (14d)$$

$$u_5^B = 2 [u_5^L - 0.25 u_2^L - 0.25 u_3^L] \quad (14e)$$

$$u_6^B = 2 [u_6^L - 0.25 u_3^L - 0.25 u_1^L] \quad (14f)$$

for computing the Dirichlet boundary conditions at the control points of the Bézier elements using the corresponding values from the Lagrange elements.

We assess the correctness of the mappings for control points and DOFs given by Eqs. (13) and (14) respectively, by solving the Laplace equation,

$$\nabla^2 u = 0 \quad (15)$$

with the analytical solution,

$$u(r, \theta) = \frac{2}{3} \left(r - \frac{1}{r} \right) \sin \theta \quad (16)$$

over a circular domain whose radial coordinate (r) and angular coordinate (θ) are bounded by $1 \leq r \leq 2$ and $0 \leq \theta \leq \pi/2$.

A circular domain is chosen so that the correctness of the mapping for control points (13) can be tested for geometries with curved edges, and the analytical solution is chosen such that the mapping for DOFs (14) can be tested for non-homogeneous Dirichlet boundary conditions. Convergence studies are performed over a set of successfully refined meshes of which the first four meshes are shown in Fig. 5. The convergence plots of error norms shown in Fig. 6 indicate that optimal convergence rates are obtained with the proposed mappings techniques for control points and DOFs.

Remark 2: It has been observed that the convergence rates obtained without applying the mapping for either the control points or DOFs or both are suboptimal.

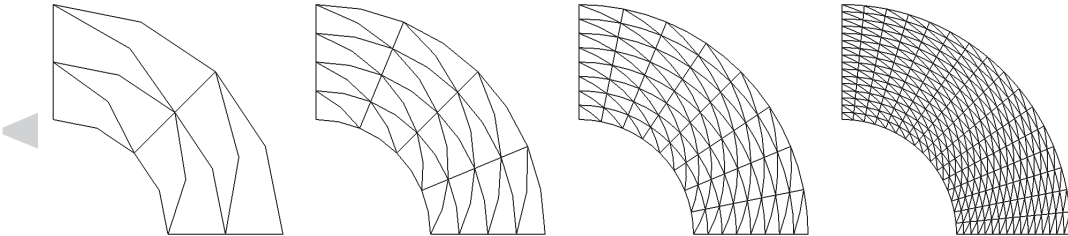


Figure 5. Laplace equation over circular annulus: first four finite element meshes used.

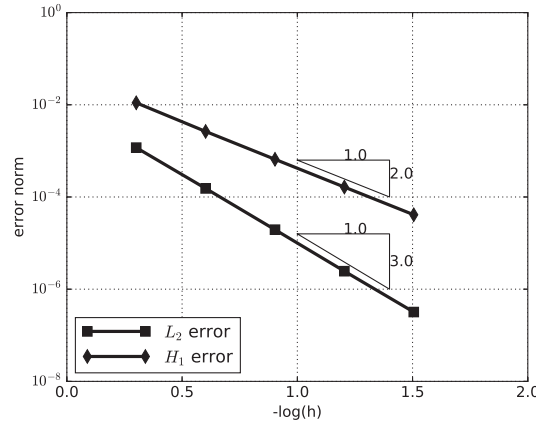


Figure 6. Laplace equation over circular annulus: convergence of L_2 and H_1 errors in the solution.

3. GOVERNING EQUATIONS - LINEAR ELASTICITY

The equations governing the elastodynamics of a linear elastic body occupying a domain Ω in the initial configuration are given by,

$$\rho \mathbf{a}(\mathbf{x}, t) - \nabla \cdot \boldsymbol{\sigma}(\mathbf{x}, t) = \mathbf{f}(\mathbf{x}, t) \quad \forall \mathbf{x} \in \Omega, t \in [0, T] \quad (17)$$

$$\mathbf{u}(\mathbf{x}, t) = \mathbf{g}(\mathbf{x}, t) \quad \forall \mathbf{x} \in \Gamma_D, t \in [0, T] \quad (18)$$

$$\boldsymbol{\sigma}(\mathbf{x}, t) \cdot \mathbf{n} = \mathbf{t}(\mathbf{x}, t) \quad \forall \mathbf{x} \in \Gamma_N, t \in [0, T] \quad (19)$$

$$\mathbf{u}(\mathbf{x}, 0) = \mathbf{u}_0(\mathbf{x}) \quad \forall \mathbf{x} \in \Omega \quad (20)$$

$$\mathbf{v}(\mathbf{x}, 0) = \mathbf{v}_0(\mathbf{x}) \quad \forall \mathbf{x} \in \Omega \quad (21)$$

where, \mathbf{x} is an arbitrary point in the domain Ω , T is the total time span, ρ is the density of the solid, \mathbf{u} is the displacement vector, $\mathbf{v}(= \frac{d\mathbf{u}}{dt})$ is the velocity vector, $\mathbf{a}(= \frac{d^2\mathbf{u}}{dt^2})$ is the acceleration vector, \mathbf{u}_0 is the initial displacement vector, \mathbf{v}_0 is the initial velocity vector, $\boldsymbol{\sigma}$ is the stress tensor, \mathbf{n} is the unit outward normal on the boundary, Γ , of Ω , \mathbf{f} is the body force, \mathbf{g} is the prescribed displacement on the Dirichlet boundary Γ_D and \mathbf{t} is the prescribed traction on the Neumann boundary Γ_N . The Dirichlet and Neumann boundaries are such that $\Gamma = \Gamma_D \cup \Gamma_N$ and $\Gamma_D \cap \Gamma_N = \emptyset$.

The stress tensor, $\boldsymbol{\sigma}$, called as the Cauchy stress, is related to strain tensor, $\boldsymbol{\varepsilon}$, by the constitutive relation,

$$\boldsymbol{\sigma} = \mathbf{D} : \boldsymbol{\varepsilon} \quad \text{or} \quad \sigma_{ij} = D_{ijkl} \varepsilon_{kl} \quad (22)$$

where,

$$\boldsymbol{\varepsilon} = \nabla^s \mathbf{u} = \frac{1}{2} (\nabla \mathbf{u} + \nabla \mathbf{u}^T) \quad \text{or} \quad \varepsilon_{ij} = \frac{1}{2} \left(\frac{\partial u_i}{\partial x_j} + \frac{\partial u_j}{\partial x_i} \right) \quad (23)$$

and \mathbf{D} is elasticity tensor of order four. With bulk modulus κ and shear modulus μ , the elasticity tensor \mathbf{D} for the isotropic and homogeneous linear elastic material is given in the component form as,

$$D_{ijkl} = \kappa \delta_{ij} \delta_{kl} + \mu (\delta_{ik} \delta_{jl} + \delta_{il} \delta_{jk} - \frac{2}{3} \delta_{ij} \delta_{kl}) \quad (24)$$

The bulk modulus (κ) and the shear modulus (μ) are related to the Young's modulus (E) and Poisson's ration (ν) as given by,

$$\kappa = \frac{E}{3(1-2\nu)}; \quad \mu = \frac{E}{2(1+\nu)}. \quad (25)$$

For mathematical convenience in Galerkin finite element formulations, strain, stress and elasticity tensors are represented in the matrix form as,

$$\boldsymbol{\varepsilon} = \left\{ \varepsilon_{xx} \quad \varepsilon_{yy} \quad \varepsilon_{zz} \quad 2\varepsilon_{xy} \quad 2\varepsilon_{yz} \quad 2\varepsilon_{zx} \right\}^T, \quad (26)$$

$$\boldsymbol{\sigma} = \left\{ \sigma_{xx} \quad \sigma_{yy} \quad \sigma_{zz} \quad \sigma_{xy} \quad \sigma_{yz} \quad \sigma_{zx} \right\}^T, \quad (27)$$

$$\mathbf{D} = 2\mu \mathbf{I}_0 + \lambda \mathbf{m} \mathbf{m}^T, \quad (28)$$

where,

$$\lambda = \kappa - \frac{2}{3}\mu, \quad (29)$$

$$\mathbf{m} = \begin{bmatrix} 1 & 1 & 1 & 0 & 0 & 0 \end{bmatrix}^T, \quad (30)$$

$$\mathbf{I}_0 = \text{diag} \left[1 \quad 1 \quad 1 \quad \frac{1}{2} \quad \frac{1}{2} \quad \frac{1}{2} \right] \quad (31)$$

4. FINITE ELEMENT FORMULATIONS

4.1. Pure displacement formulation

The pure displacement formulation, also referred to as the irreducible formulation in the finite element literature, is the standard finite element formulation in which only displacements are considered as the independent variables without any additional modifications to the governing equations or stress and strain measures. For the detailed discussion, the reader is suggested to refer to any standard textbook on basic finite element methods for solid mechanics, such as [52, 53, 54].

The virtual work statement for the governing equations (17) can be written as,

$$\int_{\Omega} \delta \mathbf{u}^T \rho \mathbf{a} \, d\Omega + \int_{\Omega} \delta \boldsymbol{\varepsilon}^T \boldsymbol{\sigma} \, d\Omega = \int_{\Omega} \delta \mathbf{u}^T \mathbf{f} \, d\Omega + \int_{\Gamma_N} \delta \mathbf{u}^T \mathbf{t} \, d\Gamma_N. \quad (32)$$

Now, considering the approximations for the actual and virtual displacement fields as,

$$\mathbf{u} = \mathbf{N}_u \mathbf{u}, \quad \delta \mathbf{u} = \mathbf{N}_u \delta \mathbf{u}, \quad (33)$$

the spatially-discretised equations for the virtual work statement (32) can be obtained as,

$$\mathbf{M} \mathbf{a} + \mathbf{F}^{\text{int,Disp}} = \mathbf{F}^{\text{ext}}, \quad (34)$$

with mass matrix, \mathbf{M} , the vector of external forces, \mathbf{F}^{ext} , and the vector of internal forces, $\mathbf{F}^{\text{int,Disp}}$, given by,

$$\mathbf{M} = \int_{\Omega} \rho \mathbf{N}_u^T \mathbf{N}_u \, d\Omega \quad (35a)$$

$$\mathbf{F}^{\text{int,Disp}} = \int_{\Omega} \mathbf{B}^T \boldsymbol{\sigma} \, d\Omega \quad (35b)$$

$$\mathbf{F}^{\text{ext}} = \int_{\Omega} \mathbf{N}_u^T \mathbf{f} \, d\Omega + \int_{\Gamma_N} \mathbf{N}_u^T \mathbf{t} \, d\Gamma \quad (35c)$$

where, \mathbf{B} is the standard strain-displacement matrix.

Now, using strain-displacement matrix, the strain tensor from Eq. (26) can be written as,

$$\boldsymbol{\varepsilon} = \mathbf{B} \mathbf{u}. \quad (36)$$

The \mathbf{B} matrix for an element with $nb f$ number of basis functions is given as,

$$\mathbf{B} = [\mathbf{B}_1, \mathbf{B}_2, \dots, \mathbf{B}_{nb f}], \quad (37)$$

where, the sub-matrix \mathbf{B}_a , for $1 \leq a \leq nb f$, for three-dimensional problem is,

$$\mathbf{B}_a = \begin{bmatrix} B_1 & 0 & 0 \\ 0 & B_2 & 0 \\ 0 & 0 & B_3 \\ B_2 & B_1 & 0 \\ 0 & B_3 & B_2 \\ B_3 & 0 & B_1 \end{bmatrix} \quad (38)$$

with

$$B_1 = \frac{\partial N_a}{\partial x}; \quad B_2 = \frac{\partial N_a}{\partial y}; \quad \text{and} \quad B_3 = \frac{\partial N_a}{\partial z}. \quad (39)$$

4.2. \mathbf{B} -bar formulation

It is now a well-established fact that the pure displacement formulation for finite elements based on linear approximation functions displays a very stiff behaviour for nearly incompressible materials, i.e., when $\nu \rightarrow 0.5$. This phenomenon is called as *locking*. Even though higher-order elements are less prone to locking, they still suffer from spurious oscillations in the stress field, as observed with the higher-order NURBS in [55, 56]. These spurious oscillations significantly deteriorate the convergence rates in displacement as well as stress fields from their optimal values as $\nu \rightarrow 0.5$. Therefore, to obtain numerical results with optimal convergence rates in both the displacement and stress fields, numerous sophisticated formulations have been proposed in the literature. Because of its simplicity and the ease of implementation, we have adopted the \mathbf{B} -bar formulation in this work.

The \mathbf{B} -bar formulation, first introduced by Hughes [57], is shown to be equivalent to the three-field *displacement-pressure-volumetric strain* formulation, refer to [52, 53] for further details, and the mean-dilatation formulation by Nagtegaal et al. [58]. The fundamental idea behind the \mathbf{B} -bar

formulation is to replace the volumetric part of the small-strain tensor with an improved estimate. Thus, the modified strain tensor is defined as,

$$\bar{\boldsymbol{\varepsilon}} = \mathbf{I}_{\text{dev}} \boldsymbol{\varepsilon} + \bar{\boldsymbol{\varepsilon}}_{\text{vol}} \quad (40)$$

where, $\bar{\boldsymbol{\varepsilon}}_{\text{vol}}$ is the improved estimate of volumetric strain and \mathbf{I}_{dev} is the deviatoric projection tensor, defined as,

$$\mathbf{I}_{\text{dev}} = \mathbf{I} - \frac{1}{3} \mathbf{m} \mathbf{m}^T \quad (41)$$

in which \mathbf{I} is the identity tensor. In this work, $\bar{\boldsymbol{\varepsilon}}_{\text{vol}}$ is evaluated as the volume-weighted average of the volumetric strain ($\boldsymbol{\varepsilon}_{\text{vol}}$) at the quadrature points.

Using the same procedure followed for the displacement formulation in Section 4.1, the discrete equations for the **B**-bar formulation can be written as,

$$\mathbf{M} \mathbf{a} + \mathbf{F}^{\text{int,Bbar}} = \mathbf{F}^{\text{ext}}. \quad (42)$$

Here, the mass matrix, \mathbf{M} and the vector of external forces, \mathbf{F}^{ext} , are same as Eq. (35a) and Eq. (35c), respectively. The vector of internal forces, $\mathbf{F}^{\text{int,Bbar}}$, is given as,

$$\mathbf{F}^{\text{int,Bbar}} = \int_{\Omega} \bar{\mathbf{B}}^T \bar{\boldsymbol{\sigma}} \, d\Omega \quad (43a)$$

where, $\bar{\boldsymbol{\sigma}}$ is the modified the Cauchy stress, computed using the relation

$$\bar{\boldsymbol{\sigma}} = \mathbf{D} \bar{\boldsymbol{\varepsilon}}, \quad (44)$$

and $\bar{\mathbf{B}}$ is the modified strain-displacement matrix. A sub-matrix of the $\bar{\mathbf{B}}$ matrix, for the 3D problem, is given as,

$$\bar{\mathbf{B}}_a = \begin{bmatrix} (\bar{B}_1 + 2B_1)/3 & (\bar{B}_2 - B_2)/3 & (\bar{B}_3 - B_3)/3 \\ (\bar{B}_1 - B_1)/3 & (\bar{B}_2 + 2B_2)/3 & (\bar{B}_3 - B_3)/3 \\ (\bar{B}_1 - B_1)/3 & (\bar{B}_2 - B_2)/3 & (\bar{B}_3 + 2B_3)/3 \\ B_2 & B_1 & 0 \\ 0 & B_3 & B_2 \\ B_3 & 0 & B_1 \end{bmatrix} \quad (45)$$

where,

$$\bar{B}_1 = \frac{1}{V^e} \int_{\Omega^e} \frac{\partial N_a}{\partial x} \, d\Omega; \quad \bar{B}_2 = \frac{1}{V^e} \int_{\Omega^e} \frac{\partial N_a}{\partial y} \, d\Omega; \quad \bar{B}_3 = \frac{1}{V^e} \int_{\Omega^e} \frac{\partial N_a}{\partial z} \, d\Omega. \quad (46)$$

in which V^e is the volume of the element in the reference configuration. For the plane-strain and axisymmetric problems, the **B**-bar matrix needs to be modified accordingly, see [53] for the details.

Remark 3: It has been observed that the convergence rates for both the displacements and stresses reduce by one order of magnitude when one-point quadrature rule is used for calculating $\bar{\epsilon}_{\text{vol}}$ and the corresponding quantities.

5. INTEGRATION IN TIME

The spatially-discretised equations (34) and (42) can be solved in time domain either explicitly or implicitly. In this work, we use a variation of the single-step explicit scheme proposed by Chung and Lee [59] for obtaining explicit solutions and the modified first-order generalised- α scheme proposed by Kadapa et al. [60] for obtaining the implicit solutions.

We consider a uniform time increment, Δt , over the whole time span of a simulation for all the numerical examples presented in this work, and we do not take damping into account. Damping can be added to the formulations considered in this work in a straightforward manner, when necessary.

For the purpose of presenting time integration schemes in a concise manner, we combine the equations (34) and (42) into the following single equation,

$$\mathbf{M} \mathbf{a} + \mathbf{F}^{\text{int}} = \mathbf{F}^{\text{ext}}, \quad (47)$$

in which \mathbf{F}^{int} is chosen accordingly depending up on the formulation.

$$\text{For the displacement formulation: } \mathbf{F}^{\text{int}} = \mathbf{F}^{\text{int,Disp}} \quad (48)$$

$$\text{For the B-bar formulation: } \mathbf{F}^{\text{int}} = \mathbf{F}^{\text{int,Bbar}} \quad (49)$$

5.1. Explicit time integration

Our experience with the central difference scheme indicates that it needs to be used with caution. As the central difference scheme has zero numerical damping, it fails to damp out spurious initial stress fields. Though this is not a serious issue for the compressible materials, it has been observed in the present work that this issue becomes quite severe in the case of nearly incompressible materials. This experience has prompted us to switch to a scheme that offers a certain amount of numerical damping.

Following [59], the explicit time integration scheme for the fully discrete version of (47) becomes,

$$\mathbf{M} \mathbf{a}_{n+1} = \mathbf{F}_n^{\text{ext}} - \mathbf{F}_n^{\text{int}} \quad (50a)$$

$$\mathbf{u}_{n+1} = \mathbf{u}_n + \Delta t \mathbf{v}_n + \Delta t^2 \left[\left(\frac{1}{2} - \beta \right) \mathbf{a}_n + \beta \mathbf{a}_{n+1} \right] \quad (50b)$$

$$\mathbf{v}_{n+1} = \mathbf{v}_n + \Delta t [(1 - \gamma) \mathbf{a}_n + \gamma \mathbf{a}_{n+1}] \quad (50c)$$

where,

$$\mathbf{F}_n^{\text{ext}} = \int_{\Omega} \mathbf{N}_u^T \mathbf{f}_n \, d\Omega + \int_{\Gamma} \mathbf{N}_u^T \mathbf{t}_n \, d\Gamma \quad (51)$$

and,

$$\text{For the displacement formulation: } \mathbf{F}_n^{\text{int}} = \int_{\Omega} \mathbf{B}^T \boldsymbol{\sigma}_n \, d\Omega \quad (52)$$

$$\text{For the } \mathbf{B}\text{-bar formulation: } \mathbf{F}_n^{\text{int}} = \int_{\Omega} \bar{\mathbf{B}}^T \bar{\boldsymbol{\sigma}}_n \, d\Omega \quad (53)$$

Chung and Lee [59] proved that the explicit scheme given by equations (50) is second-order accurate for

$$\gamma = 3/2 \quad \text{and} \quad 1 \leq \beta \leq 28/27, \quad (54)$$

and that the scheme becomes spectrally identical to the central difference scheme for $\beta = 1$. It was also shown that the scheme possesses certain amount of numerical damping for $\beta > 1$.

In this work, we choose

$$\gamma = 3/2 \quad \text{and} \quad \beta = \frac{13}{12}, \quad (55)$$

for which it can be proven through spectral analysis that the scheme becomes *third-order accurate for the undamped case* and still offers a sufficient amount of numerical damping to damp out the initial spurious oscillations in the stress field particularly for the nearly incompressible case.

For computationally efficient solution of equations (50), lumped mass matrices are commonly used in explicit elastodynamic analyses. Using the row-sum lumping, we get the lumped-mass matrix for the quadratic Bézier triangular and tetrahedral elements as,

$$\mathbf{M}^{e,\text{tria}} = \frac{\rho V^e}{6} \quad \text{diag}[\mathbf{1}_6 \quad \mathbf{1}_6] \quad (56)$$

$$\mathbf{M}^{e,\text{tetra}} = \frac{\rho V^e}{10} \quad \text{diag}[\mathbf{1}_{10} \quad \mathbf{1}_{10} \quad \mathbf{1}_{10}] \quad (57)$$

where, V^e is the volume of the element, $\mathbf{1}_6 = [1 \ 1 \ 1 \ 1 \ 1 \ 1]$ and $\mathbf{1}_{10} = [1 \ 1 \ 1 \ 1 \ 1 \ 1 \ 1 \ 1 \ 1 \ 1]$.

5.2. Implicit time integration

Using the modified first-order generalised- α scheme of [60] for the implicit solutions of Eq. (47), we get,

$$\mathbf{M} \mathbf{a}_{n+\alpha_m} + \mathbf{K} \mathbf{u}_{n+\alpha_f} = \mathbf{F}_{n+\alpha_f}^{\text{ext}} \quad (58)$$

where,

$$\mathbf{a}_{n+\alpha_m} = \alpha_m \mathbf{a}_{n+1} + (1 - \alpha_m) \mathbf{a}_n \quad (59)$$

$$\mathbf{u}_{n+\alpha_f} = \alpha_f \mathbf{u}_{n+1} + (1 - \alpha_f) \mathbf{u}_n \quad (60)$$

$$\mathbf{F}_{n+\alpha_f}^{\text{ext}} = \alpha_f \mathbf{F}_{n+1}^{\text{ext}} + (1 - \alpha_f) \mathbf{F}_n^{\text{ext}} \quad (61)$$

and the stiffness matrix \mathbf{K} is,

$$\text{For the displacement formulation: } \mathbf{K} = \int_{\Omega} \mathbf{B}^T \mathbf{D} \mathbf{B} \, d\Omega, \quad (62)$$

$$\text{For the } \mathbf{B}\text{-bar formulation: } \bar{\mathbf{K}} = \int_{\Omega} \bar{\mathbf{B}}^T \mathbf{D} \bar{\mathbf{B}} \, d\Omega. \quad (63)$$

Once the Eq. (58) is solved for displacement, \mathbf{u}_{n+1} , other solution variables at time instant t_{n+1} can be evaluated using the relations,

$$\mathbf{v}_{n+1} = \frac{\alpha_m}{\alpha_f \gamma \Delta t} (\mathbf{u}_{n+1} - \mathbf{u}_n) + \frac{(\alpha_f - 1)}{\alpha_f} \mathbf{v}_n + \frac{(\gamma - \alpha_m)}{\gamma \alpha_f} \dot{\mathbf{u}}_n \quad (64)$$

$$\mathbf{a}_{n+1} = \frac{\alpha_m}{\alpha_f \gamma^2 \Delta t^2} (\mathbf{u}_{n+1} - \mathbf{u}_n) - \frac{1}{\alpha_f \gamma \Delta t} \mathbf{v}_n + \frac{\gamma - 1}{\gamma} \mathbf{a}_n + \frac{(\gamma - \alpha_m)}{\alpha_f \gamma^2 \Delta t} \dot{\mathbf{u}}_n \quad (65)$$

$$\dot{\mathbf{u}}_{n+1} = \frac{1}{\gamma \Delta t} (\mathbf{u}_{n+1} - \mathbf{u}_n) + \frac{\gamma - 1}{\gamma} \dot{\mathbf{u}}_n \quad (66)$$

The implicit time integration scheme used in the present work is unconditionally stable and second-order accurate, provided,

$$\alpha_f = \frac{1}{1 + \rho_{\infty}}; \quad \alpha_m = \frac{3 - \rho_{\infty}}{2(1 + \rho_{\infty})}; \quad \gamma = \frac{1}{2} + \alpha_m - \alpha_f; \quad \text{for } 0 \leq \rho_{\infty} \leq 1, \quad (67)$$

where, ρ_{∞} is the spectral radius at an infinite time step. ρ_{∞} allows to control the amount of numerical damping. For further details, we refer the reader to [60].

6. NUMERICAL EXAMPLES - SPATIAL CONVERGENCE STUDIES

In all the numerical examples presented in this work, the element stiffness matrix and internal force vectors are evaluated using 3-point Gauss quadrature rule for triangular elements and 4-point rule for tetrahedral elements. All the 3D meshes and 2D unstructured meshes used in the present work are generated using the student version of HyperMesh [61]. Nodal stress plots are produced using the stress recovery technique of extrapolation from the quadrature points.

For convenience in the discussion of results, we denote various elements considered in this work using the following abbreviations:

TRI3	- 3-noded triangular element with pure displacement formulation.
TRIB6	- 6-noded Bézier triangular element with pure displacement formulation.
TRIB6B	- 6-noded Bézier triangular element with \mathbf{B} -bar formulation.
TET4	- 4-noded tetrahedral element with pure displacement formulation.
TETB10	- 10-noded Bézier tetrahedral element with pure displacement formulation.
TETB10B	- 10-noded Bézier tetrahedral element with \mathbf{B} -bar formulation.

Before presenting the spatial convergence studies, we first establish the *inf-sup* stability of the \mathbf{B} -bar formulation considered in this work. The *inf-sup* values are computed numerically for the

circular annulus problem depicted in Fig. 8 using the methodology proposed by Chapelle and Bathe [62]. The values of numerical *inf-sup* constant (β_h) shown in Fig. 7 demonstrate a clear convergence towards a constant value as the mesh is refined, indicating that the formulation is *inf-sup* stable.

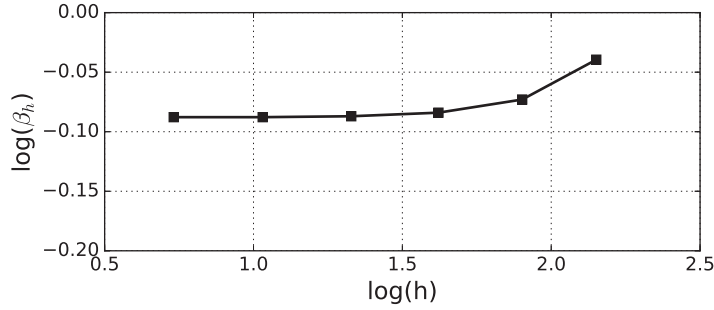


Figure 7. Thick-walled cylinder: numerical *inf-sup* constant (β_h) Versus mesh size (h).

Remark 4: For elastostatic problems, **B**-bar quadratic Lagrange elements produce identical results to those of quadratic Bézier elements. For the sake of brevity and since quadratic Lagrange elements are not amenable for explicit schemes, the results obtained with quadratic Lagrange elements are not reported in this paper.

6.1. Spatial convergence in 2D - thick-walled cylinder under internal pressure

In this example, we assess the spatial convergence of the proposed triangular elements using the example of a thick-walled cylinder subjected to internal pressure load. This example has been studied in Kadapa et al. [56] to assess the spatial convergence of NURBS based IGA. Due to the symmetry in geometry and loading conditions of the problem, only a quarter portion is considered for the analysis, as shown in the Fig. 8, and is modelled with the plane-strain assumption. Due to the circular geometries involved, this problem serves as a good example to demonstrate the performance of the proposed elements for curved shapes.

Analytical solutions for the radial displacement, d_r , hoop stress, $\sigma_{\theta\theta}$, radial stress, σ_{rr} , and shear stress, $\tau_{r\theta}$, given by the following equations are used in computing the error norms.

$$d_r = \frac{p r_i^2}{(r_o^2 - r_i^2) E} \left[(1 - \nu - 2\nu^2) r + (1 + \nu) \frac{r_o^2}{r} \right] \quad (68)$$

$$\sigma_{rr} = \frac{p r_i^2}{r_o^2 - r_i^2} \left[1 - \frac{r_o^2}{r^2} \right] \quad (69)$$

$$\sigma_{\theta\theta} = \frac{p r_i^2}{r_o^2 - r_i^2} \left[1 + \frac{r_o^2}{r^2} \right] \quad (70)$$

$$\tau_{r\theta} = 0 \quad (71)$$

where r is the radius at an arbitrary point in the domain.

The spatial convergence studies are performed for the successively refined meshes as shown in Fig. 5, and the error norms for three different values of Poisson's ratio, $\nu = 0.3$, $\nu = 0.48$ and

$\nu = 0.49999$ are plotted in Figs. 9 and 10, respectively, for the displacement and **B**-bar formulation. For comparison, the results obtained with the TRI3 element are also presented. These graphs illustrate that while the convergence rates for the TRIB6 element deteriorate as $\nu \rightarrow 0.5$, the convergence rates obtained with the TRIB6B element are always optimal and are independent of the value of Poisson's ratio. Moreover, even for the compressible material, the magnitude of errors obtained with TRIB6 and TRIB6B is at least two orders lower than those obtained with the TRI3 element; thus, indicating that extremely accurate results can be obtained with very coarse meshes using quadratic elements. This ability to obtain accurate results with very coarse meshes results in significant savings in computational time and resources for large 3D problems, as demonstrated in the latter part of this article with elastodynamics in three dimensions.

Another interesting point to note from the convergence plots and contour plots displayed in Figs. 11 and 12 is that the pure displacement formulation is sufficient enough to obtain accurate results for the values of Poisson's ratio up to 0.48.

Having established the optimal spatial convergence rates for structured meshes, we now demonstrate the robustness of the proposed elements for unstructured meshes. We assess the spatial convergence of the proposed elements for this example using a set of unstructured meshes as shown in Fig. 13. The graphs of error norms in displacement and stress presented in Fig. 15 illustrate that the convergence rates for the **B**-bar formulation remain optimal for unstructured meshes. Moreover, the convergence rates for the displacement formulation, as shown in Fig. 14, also remain almost optimal. This is attributed to the fact the unstructured meshes have straight edges for all the internal elements as opposed to curved edges in the structured meshes in Fig. 5, which can be substantiated from the smooth contours for the internal elements presented in Fig. 16.

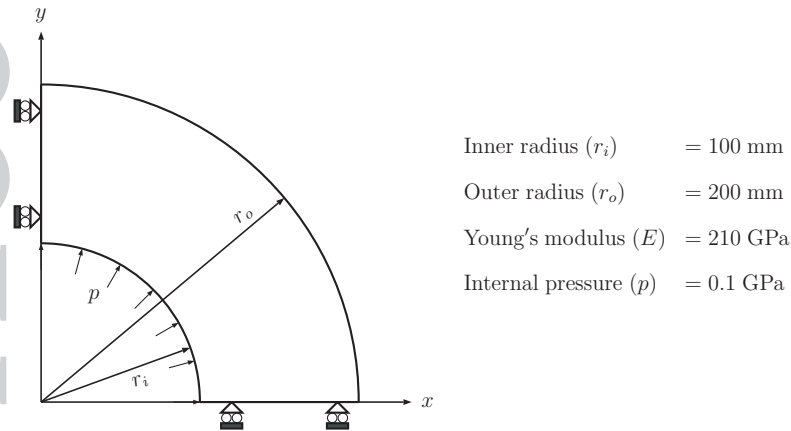


Figure 8. Thick-walled cylinder: geometry and boundary conditions.

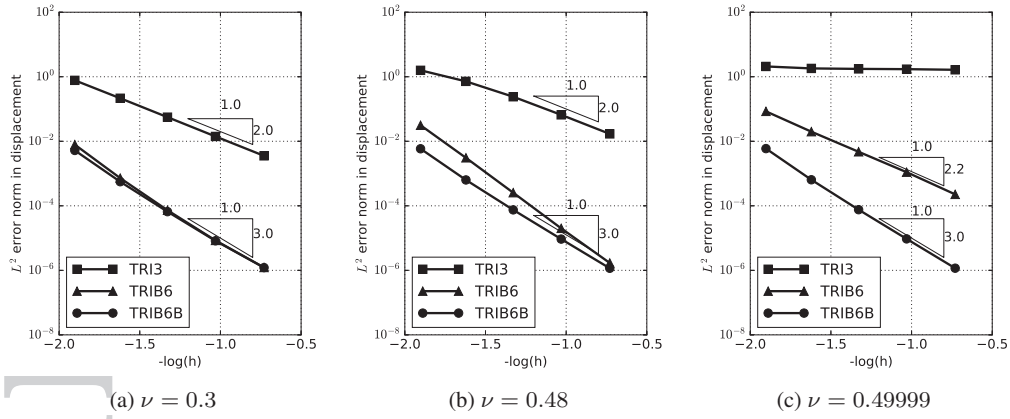


Figure 9. Thick-walled cylinder: error norm in displacement for the structured meshes.

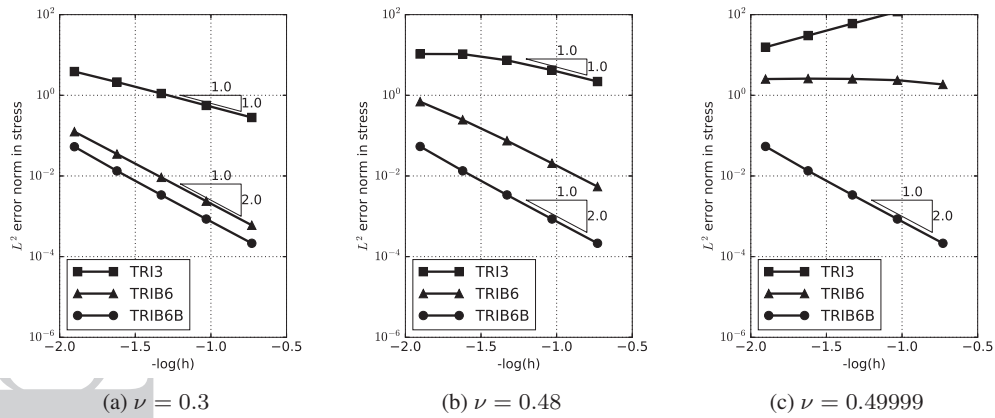
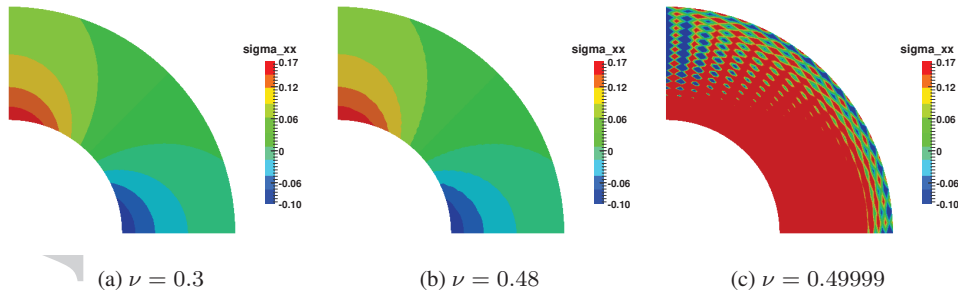


Figure 10. Thick-walled cylinder: error norm in stress for the structured meshes.

Figure 11. Thick-walled cylinder: contour plots of σ_{xx} obtained with 16×16 mesh with displacement formulation.

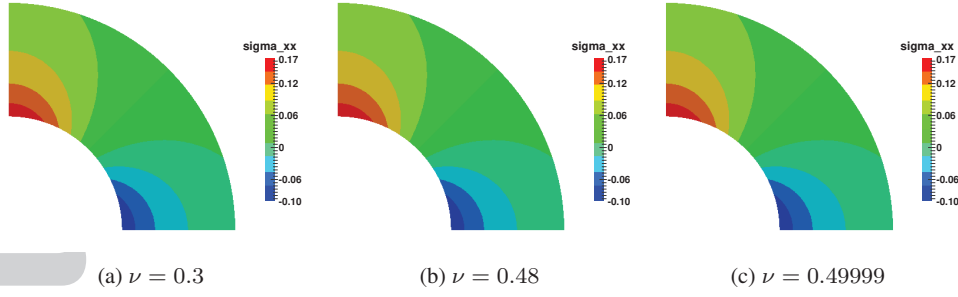
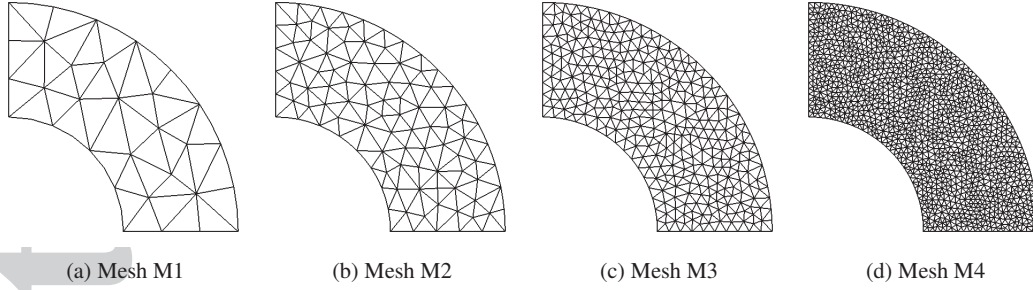
Figure 12. Thick-walled cylinder: contour plots of σ_{xx} obtained with 16×16 mesh with B-bar formulation.

Figure 13. Thick-walled cylinder: unstructured meshes.

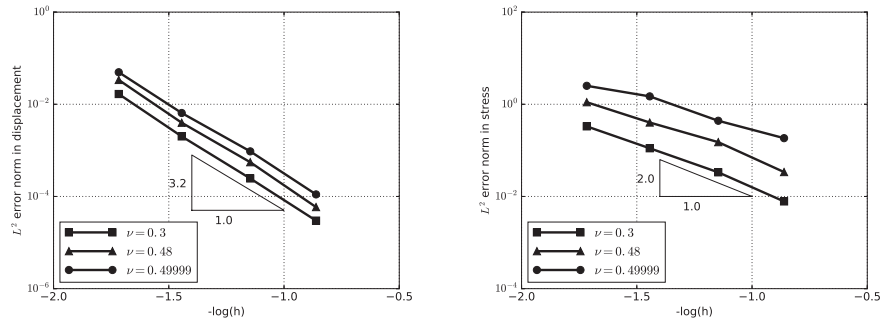


Figure 14. Thick-walled cylinder: error norms for the unstructured meshes using displacement formulation.

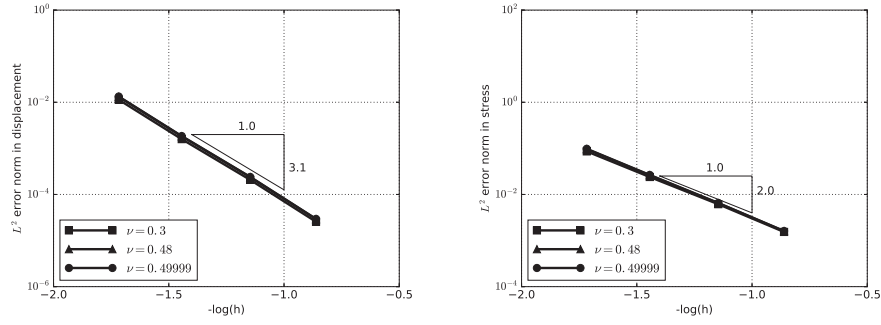


Figure 15. Thick-walled cylinder: error norms for the unstructured meshes using **B**-bar formulation.

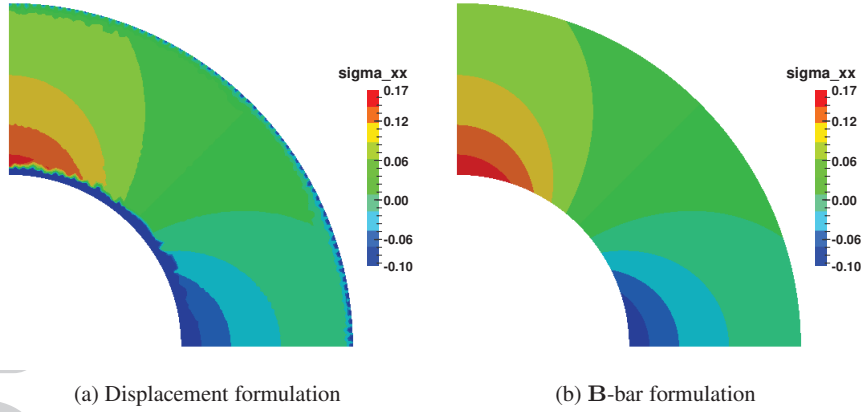


Figure 16. Thick-walled cylinder: contour plots of σ_{xx} obtained with M4 mesh.

6.2. Spatial convergence in 3D - thick-walled sphere under internal pressure

In this example we assess the spatial convergence of the proposed tetrahedral elements using the problem of a thick-walled sphere subjected to a uniform internal pressure. The spherical geometry is chosen in order to demonstrate the optimality of the convergence rates for three-dimensional geometries with curved surfaces. Due to symmetry of the geometry and boundary conditions, only 1/8th of the sphere is considered for the analysis. Error norms in displacement and stress are computed over the discretisations shown in Fig. 17 for three different values of Poisson's ratio, $\nu = \{0.3, 0.48, 0.49999\}$. From the graphs of error norms in displacement and stress shown, respectively, in Figs. 18 and 19, it can be observed that optimal convergence rates are obtained with the **B**-bar formulation for all the values of Poisson ratio considered; and the contour plots presented in Fig. 21 illustrate smooth stress contours obtained with the **B**-bar formulation as opposed to spurious oscillations with the displacement formulation presented in Fig. 20.

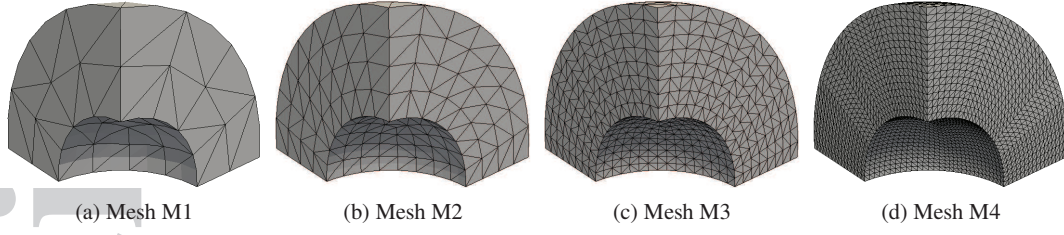


Figure 17. Thick-walled sphere: meshes used for the analysis.

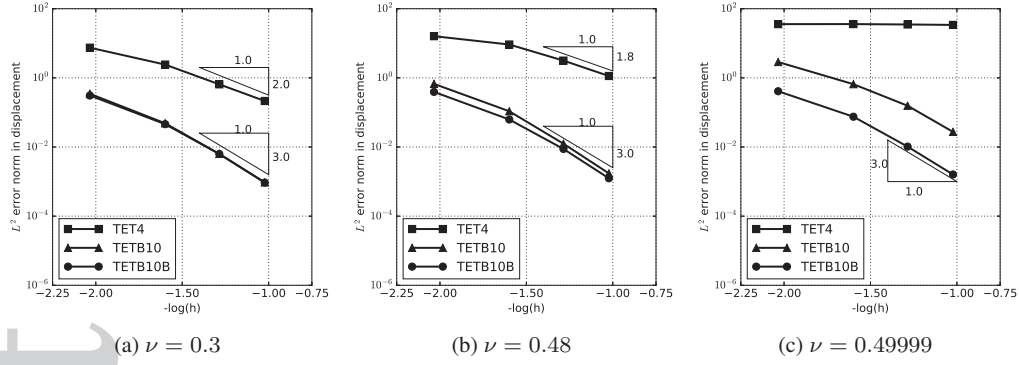


Figure 18. Thick-walled sphere: error norm in displacement.

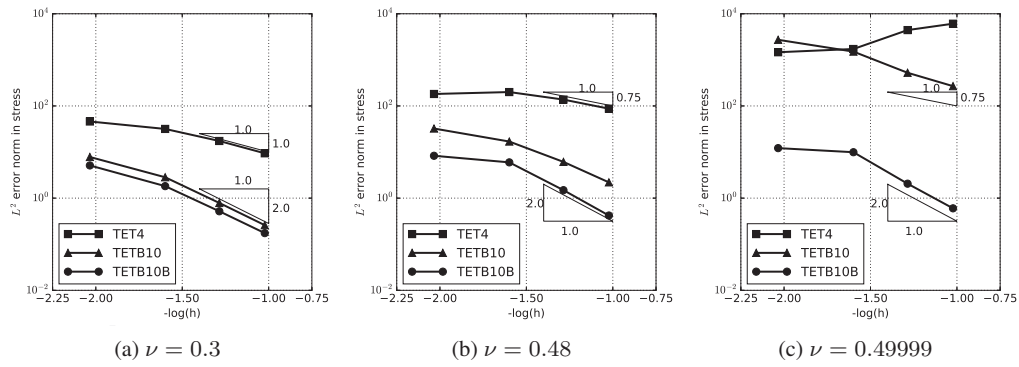


Figure 19. Thick-walled sphere: error norm stress.

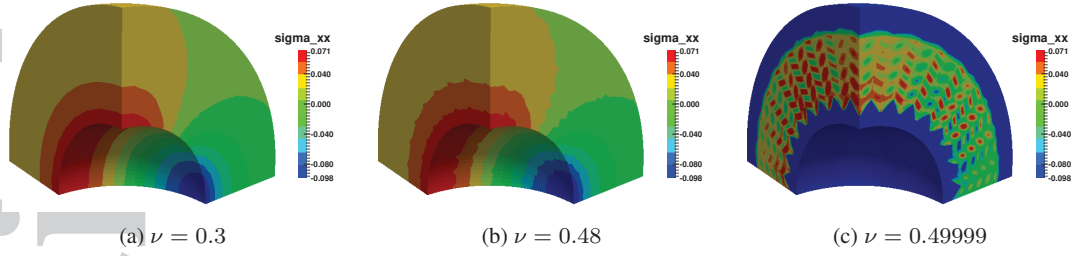


Figure 20. Thick-walled sphere: contour plots of σ_{xx} stress obtained with M3 mesh with displacement formulation (TETB10 elements).

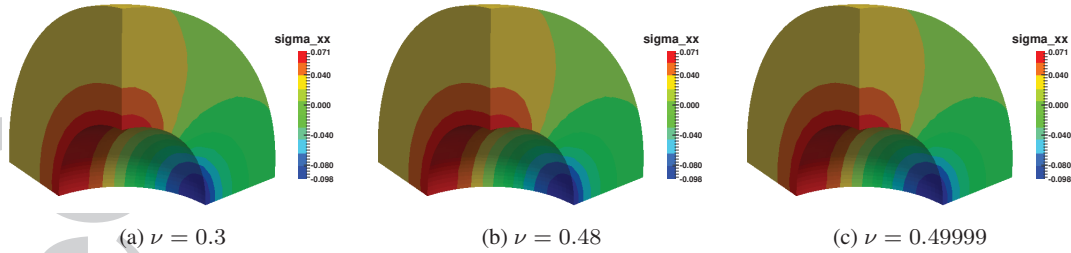


Figure 21. Thick-walled sphere: contour plots of σ_{xx} stress obtained with M3 mesh with \mathbf{B} -bar formulation (TETB10B elements).

6.3. Cook's membrane - bending behaviour in 2D

In this example, we study the bending behaviour of the proposed elements using the example of Cook's membrane. The geometry and boundary conditions of the problem are as shown in Fig. 22a. The Young's modulus of the material is $E = 240.565$ MPa, the applied force is $F = 100$ N/mm, and the plane-strain condition is assumed. The analysis is performed over successively refined meshes, shown in Fig. 22b, for the compressible ($\nu = 0.3$) and nearly incompressible ($\nu = 0.4999$) cases and the values of the Y-displacement of point A obtained with TRI3, TRIB6 and TRIB6B elements are plotted against mesh size in Fig. 23. These graphs indicate clear convergence behaviour of the proposed elements. It can also be observed that, for the nearly incompressible case, the displacements obtained with the TRIB6 elements are significantly better than those obtained with TRI3 elements. The only drawback of the pure displacement formulation is spurious oscillations in the stress field in the nearly incompressible case, which is remedied by using the \mathbf{B} -bar formulation, as demonstrated in Fig. 24 with the contour plots of pressure. This behaviour is consistent with the observations made with higher-order NURBS in Kadapa et al. [56].

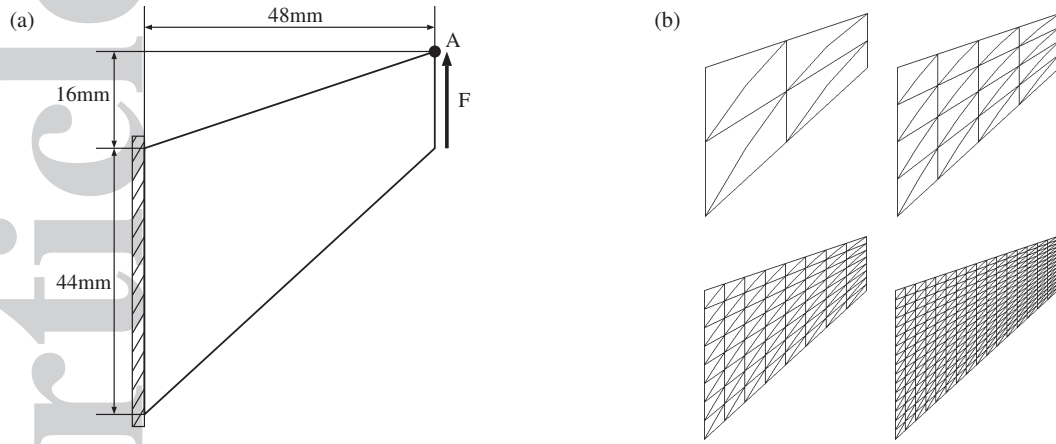
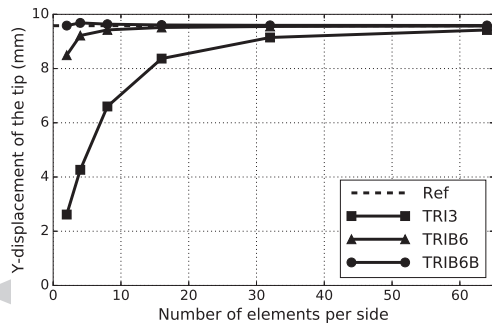
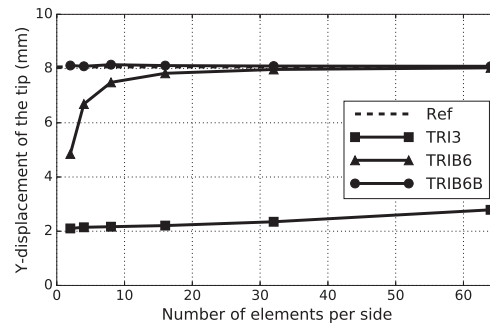


Figure 22. Cook's membrane: (a) geometry and boundary conditions and (b) first four meshes used for the analysis.



(a) $\nu = 0.3$



(b) $\nu = 0.4999$

Figure 23. Cook's membrane: convergence of the vertical displacement of point A. The reference solution is obtained with NURBS-based isogeometric analysis presented in [56].

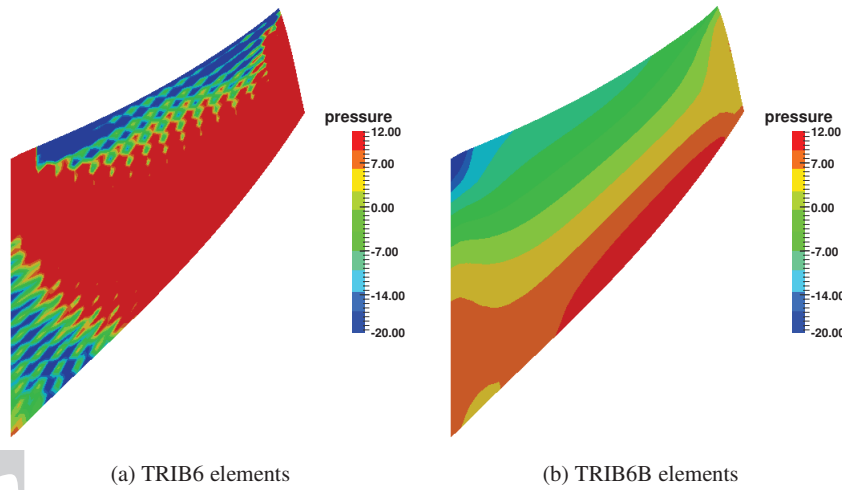


Figure 24. Cook's membrane: contour plots of pressure with 16×16 mesh for $\nu = 0.4999$.

6.4. Long tapered beam - bending behaviour in 3D

In this example, we assess the bending behaviour of the proposed elements in 3D using the example of a long tapered cantilever beam for which the geometry and boundary conditions are as shown in Fig. 25. The Young's modulus and Poisson's ratio are the same as those used for the 2D Cook's membrane problem. Simulations are performed with TET4, TETB10 and TETB10B elements over the uniformly refined meshes shown in Fig. 26 for a traction load, $\mathbf{t} = (0.0, 2.0, 0.4)$, on the face of the free end of the beam. The values of Y-displacement of point A plotted against the number of elements along the length of the beam in Fig. 27 illustrate clear convergence for the proposed elements. The contour plots presented in Fig. 28 show the smooth pressure field obtained with the B-bar formulation as opposed to the pressure field with the spurious oscillations obtained with the displacement formulation. At this point, it is important to point out the robustness of the proposed scheme in obtaining accurate numerical solutions using meshes consisting of elements with significantly higher aspect ratios.

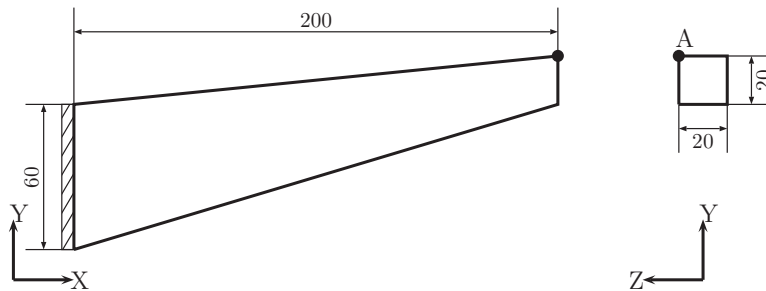


Figure 25. Long tapered beam in 3D: geometry and boundary conditions.

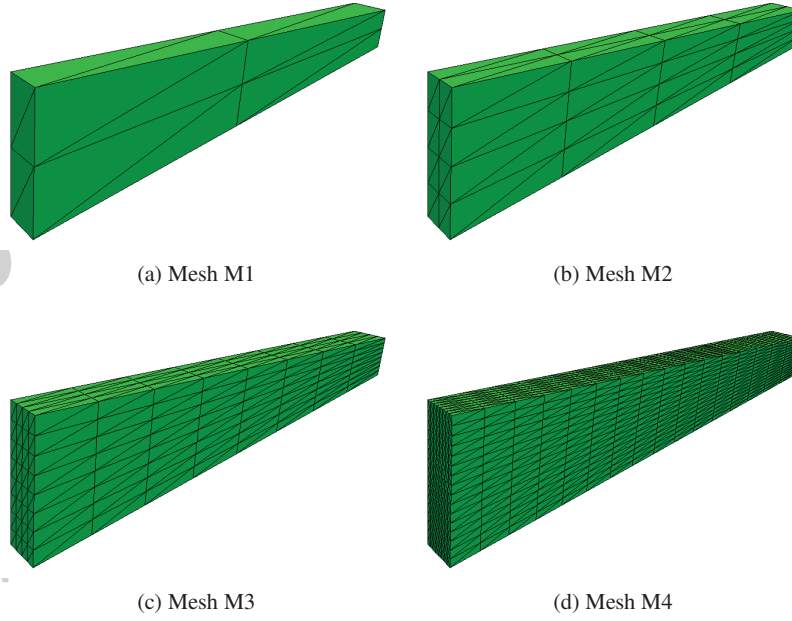


Figure 26. Long tapered beam in 3D: finite element meshes used for the analysis.

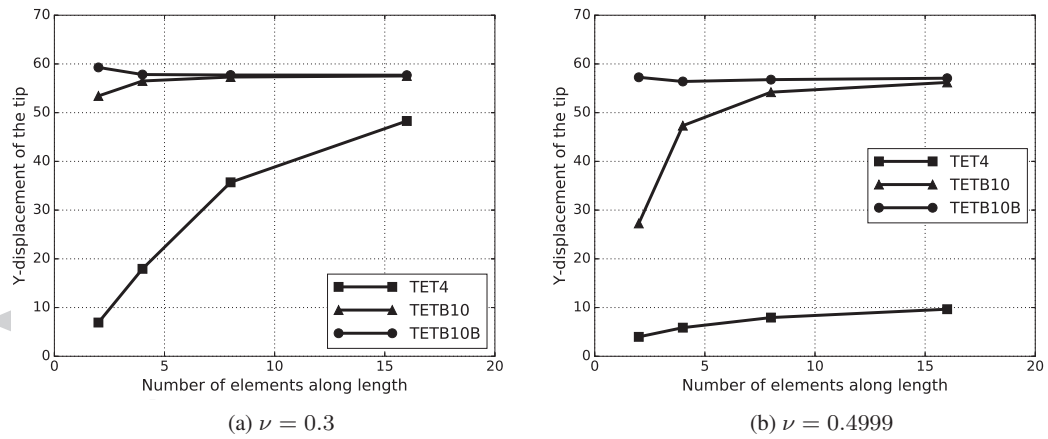


Figure 27. Long tapered beam in 3D: convergence of Y-displacement of point A.

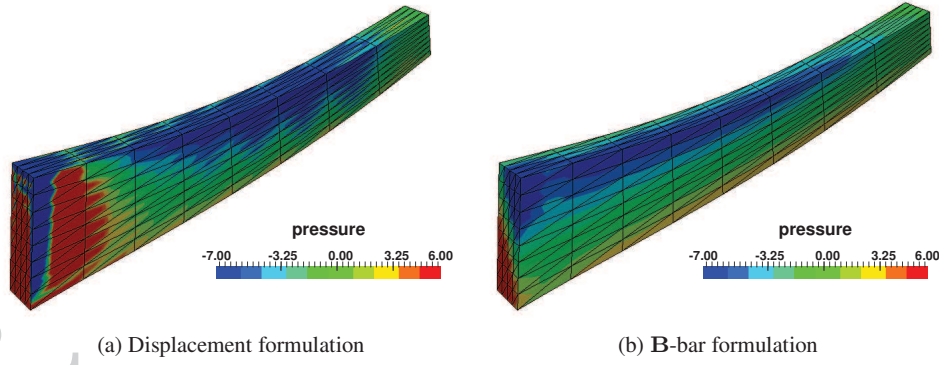


Figure 28. Long tapered beam in 3D: contour plots of pressure obtained with mesh M3 for $\nu = 0.4999$.

7. NUMERICAL EXAMPLES - ELASTODYNAMICS

Having established the spatial convergence of the proposed elements, we now present numerical examples for elastodynamics. For the implicit scheme, the spectral radius is, $\rho_\infty = 1$, and the time step is chosen sufficiently small enough. For the explicit scheme, Δt is computed based on the bulk wave speed (c) by using the formula,

$$\Delta t = \frac{\text{CFL } h}{c} \quad \text{with} \quad c = \sqrt{\frac{\kappa + 4\mu/3}{\rho}} \quad (72)$$

where, h is the characteristic length which is taken as the minimum edge length for TRI3 and TET4 elements and half of the minimum edge length for Bézier elements, and CFL is the Courant-Friedrichs-Lewy number. In all the explicit dynamic simulations presented in this work, CFL number is taken as 0.75 so that the explicit scheme is always stable.

For all the elastodynamic simulations, Young's modulus and the density of the material are $E = 210 \text{ GPa}$ and $\rho = 8000 \text{ kg/m}^3$, unless otherwise specified.

7.1. Modal analysis in 2D - cantilever beam

Before presenting the results of elastodynamic simulations, we first assess the natural frequencies of a simple cantilever beam of length 200 mm and thickness 10 mm. The Poisson's ratio is taken as 0.3, and the plane-strain condition is assumed so that the performance of TRIB6B elements can also be compared. Sample meshes considered for the analysis are shown in Fig. 29. The values of the first natural frequency of the beam obtained with different elements for different mesh densities are plotted in Fig. 30. This graph indicates clear convergence and also shows that the values obtained for the coarse meshes with the quadratic Bézier elements are much more accurate. It can also be observed that the natural frequencies for the B-bar formulation converge from below which is due to the fact that the B-bar underestimates the element stiffness. Owing to this, transient solutions obtained for the coarse meshes using the B-bar formulation have elongated time periods which, however, disappear with the mesh refinement.

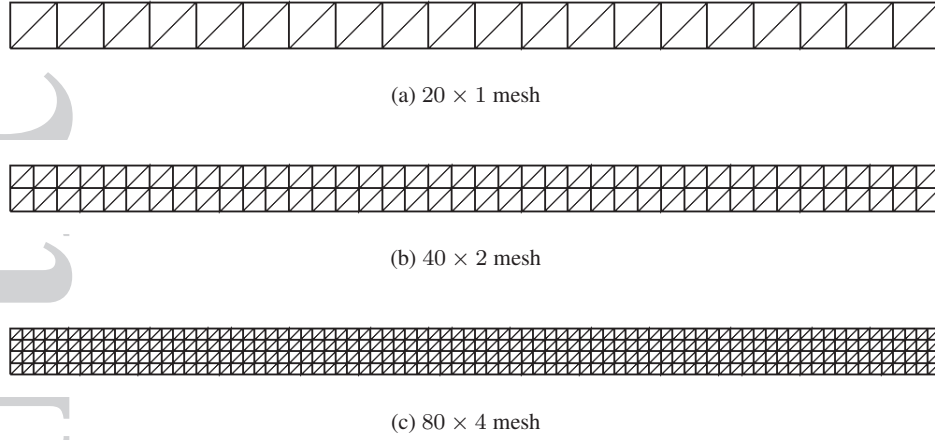


Figure 29. Cantilever beam in 2D: first three finite element meshes.

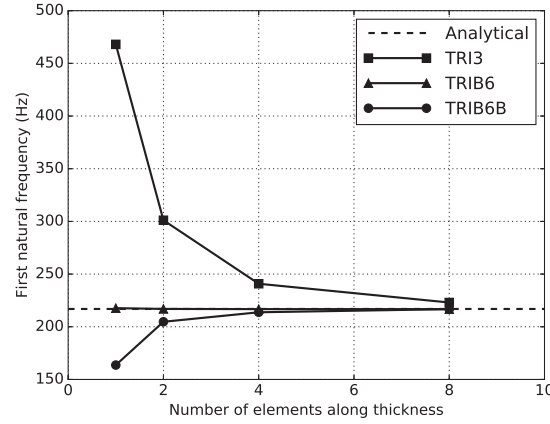


Figure 30. Cantilever beam in 2D: First natural frequency of the beam obtained with the different mesh densities using TRI3, TRIB6 and TRIB6B elements.

7.2. Elastodynamics in 2D - cantilever beam

In this example, we study the elastodynamics of a simple cantilever beam considered in the above example. The beam is excited with a uniform initial velocity of 5 m/s in the vertical direction. The dynamic behaviour of the beam is studied by monitoring the vertical displacement of the midpoint of the free end of the beam. The numerical solution obtained with the implicit scheme with 320×16 TRIB6 elements and a constant time step of $\Delta t = 5.0 \times 10^{-5}$ is used as the reference solution. The evolution of Y-displacement of the midpoint of the free end of the beam obtained from different simulations is presented in Figs. 31-33. From these graphs, it can be observed that

- The solution obtained with the TRIB6 and TRIB6B elements converge with mesh refinement, as shown in Fig. 31.
- For all the mesh densities, and for both the formulations, the solution obtained with the explicit scheme agree well with the one obtained with the implicit scheme as shown in Fig. 32 for 40×2 and 80×4 meshes. Moreover, explicit solutions for different densities

presented in Fig. 31 indicate that accurate solutions for explicit elastodynamic problems can be obtained with very coarse meshes using the TRIB6 and TRIB6B elements whereas, with TRI3 elements, very fine meshes are required to get reasonably accurate solutions, as demonstrated in Fig. 33.

Quantification of computational efficiency: TRIB6-40x2 mesh with 160 elements and 800 DOFs gives better numerical results than the TRI3-320x16 mesh with 10240 elements and 10880 DOFs, i.e., with 64 times fewer elements and 13.6 times fewer DOFs. Moreover, as the stable time step size for the explicit scheme is directly proportional to the size of the element, additional computational efficiency can be gained by using very coarse meshes in explicit dynamic simulations. Hence, the overall computational efficiency that can be achieved using the proposed elements is at least one order of magnitude lower than that of using TRI3 elements. Such significant gains in the overall computational efficiency will have a considerable impact on large-scale elastodynamic simulations for practical engineering applications.

Use of multiple quadrature points for each element may seem computationally expensive at the first look. However, close observations reveal that this cost is not as significant as it might seem. This is because, for the same number of nodes in structured meshes in 2D, one TRIB6 element is replaced by four TRI3 elements; therefore, while a total of four quadrature points are used for the four TRI3 elements, only three quadrature points are used for the TRIB6 element. The computational overhead of using multiple quadrature points becomes even less significant for problems in 3D because, one TETB10 element is replaced by at least eight TET4 elements; therefore, only four quadrature points are used for the TETB10 element in contrast to at least eight quadrature points for the TET4 elements. Moreover, it has been demonstrated that the results obtained with $a \times b$ mesh with TRIB6 elements are significantly more accurate than those obtained with the $2a \times 2b$ mesh with TRI3 elements. Thus, the ability to obtain accurate numerical results with very coarse meshes significantly outweighs the cost of using multiple quadrature points. Furthermore, whatever the additional cost incurred in the B-bar formulation is outweighed by the fact that extremely accurate results can be obtained with very coarse meshes, even for the nearly incompressible case, as demonstrated with the examples in the later part of this article.

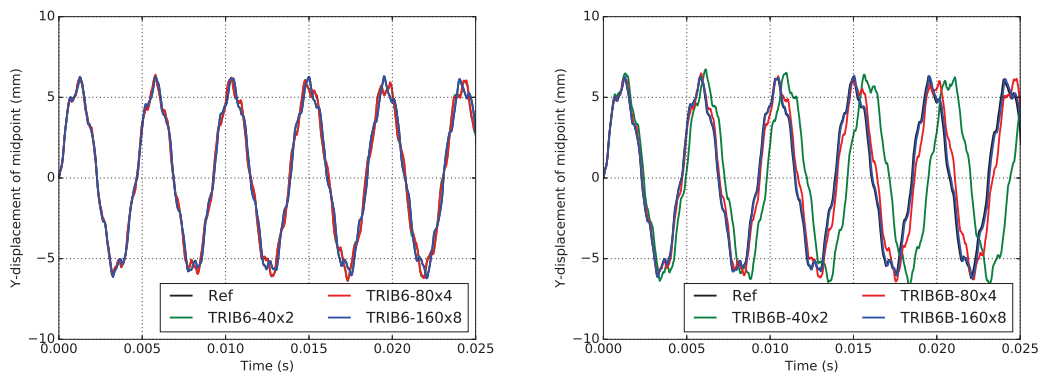


Figure 31. Cantilever beam in 2D: evolution of Y-displacement using TRIB6 and TRIB6B elements and the explicit scheme.

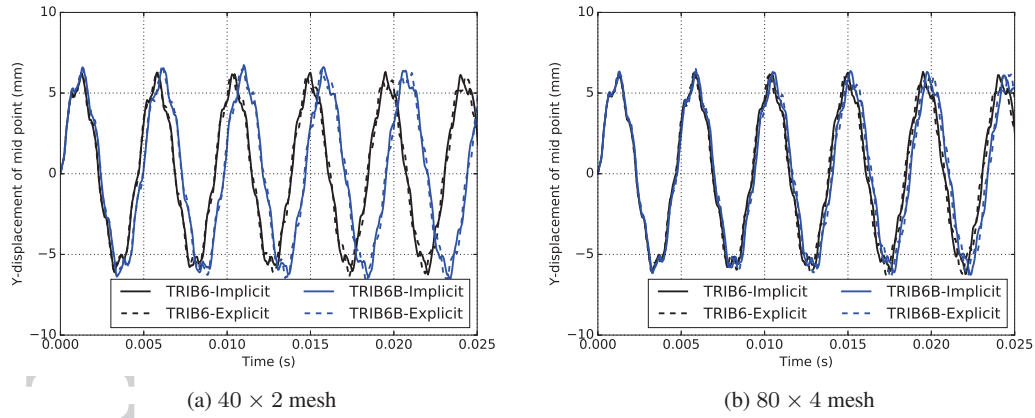


Figure 32. Cantilever beam in 2D: evolution of Y-displacement of the midpoint of the free end.

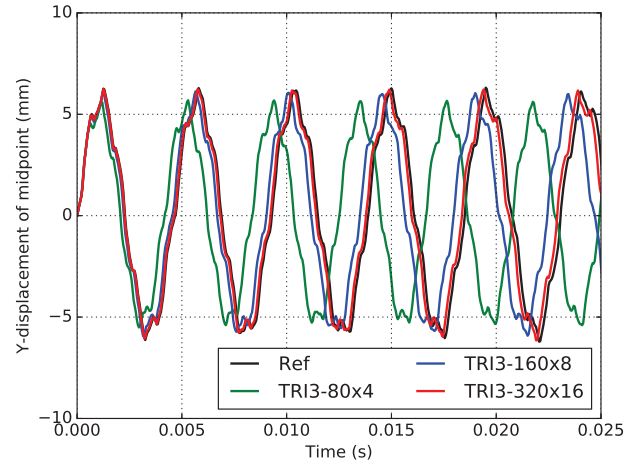


Figure 33. Cantilever beam in 2D: evolution of Y-displacement using TRI3 elements and the explicit scheme.

7.3. Elastodynamics in 2D - mechanical component

To demonstrate the applicability of the proposed elements to problems involving complex geometries, in this example, we consider a mechanical component, called the jig, whose geometry is as shown in Fig. 34. The setup of the problem is such that the leftmost edges of the component are fixed, and a uniform velocity of 5 m/s is applied as the initial velocity. The problem is assumed to be in plane-strain. The Poisson's ratio of the material is assumed to be $\nu = 0.49999$. Simulations are performed using three different meshes shown in Fig. 35 to assess the convergence. Meshes M2 and M3 are obtained as the successive refinements of mesh M1. The number of elements in the three meshes is 995, 3980 and 15920, respectively. For TRI3 elements the total number of DOFs for all the three meshes are $\{1174, 4352, 16678\}$, and the corresponding values for TRIB6 and TRIB6B elements are $\{4352, 16678, 65210\}$.

The evolution of Y-displacement of the top right corner (point A in Fig. 34) obtained from different simulations is plotted in Figs. 36 and 37. Numerical solutions obtained with the explicit

scheme match well with those obtained with the implicit scheme for all the meshes with both the displacement and **B**-bar formulations, as illustrated in Fig. 36 for the mesh M1. Fig. 37a not only shows a clear convergence of the results obtained with the proposed elements but also illustrates that the proposed elements produce very accurate results even with the coarsest mesh (M1); TRI3 elements come nowhere close to the reference solution, even with the densest mesh (M3), as shown in Fig. 37b.

The only disadvantage of the TRIB6 elements is spurious oscillations in the stress field, and this can be remedied by using the **B**-bar formulation, as demonstrated in Figs. 38 and 39 with the contour plots of σ_{xx} stress obtained for the mesh M1 at two different time instants. Therefore, whatever the additional cost incurred in the **B**-bar formulation is completely outweighed by the fact that extremely accurate results can be obtained with very coarse meshes, thus reducing the overall computational cost of the simulation as well as providing the means to perform large-scale explicit elastodynamic simulations using fewer computational resources.

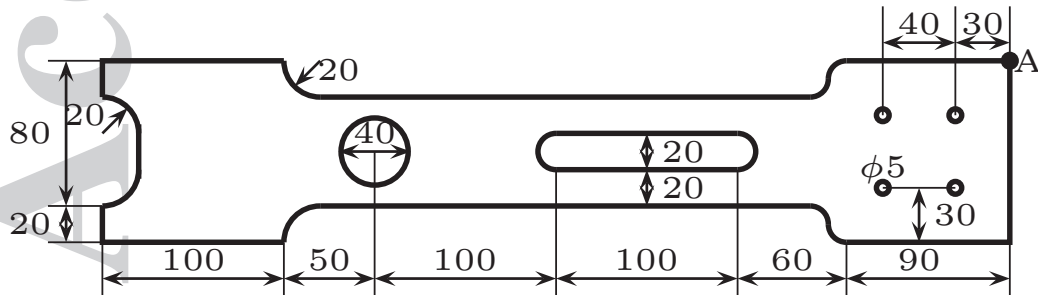


Figure 34. 2D jig: geometry of the problem. All the dimensions are in millimetres.

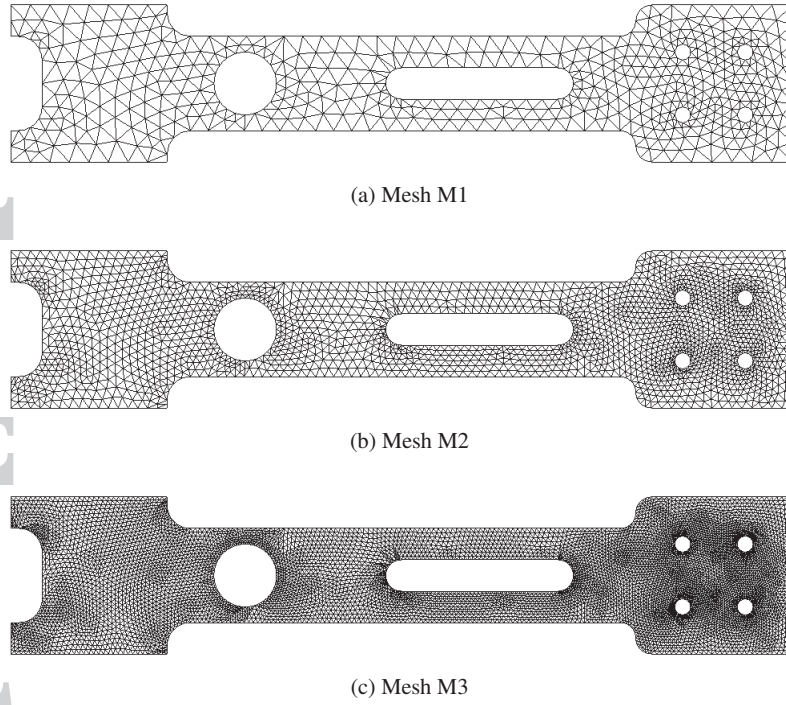


Figure 35. 2D jig: finite element meshes considered for the analysis.

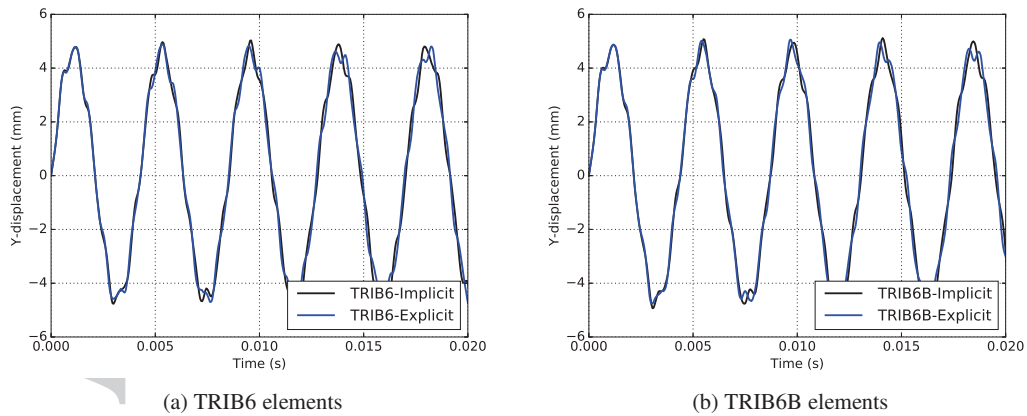


Figure 36. 2D jig: evolution of Y-displacement of point A obtained with the mesh M1 using implicit and explicit schemes.

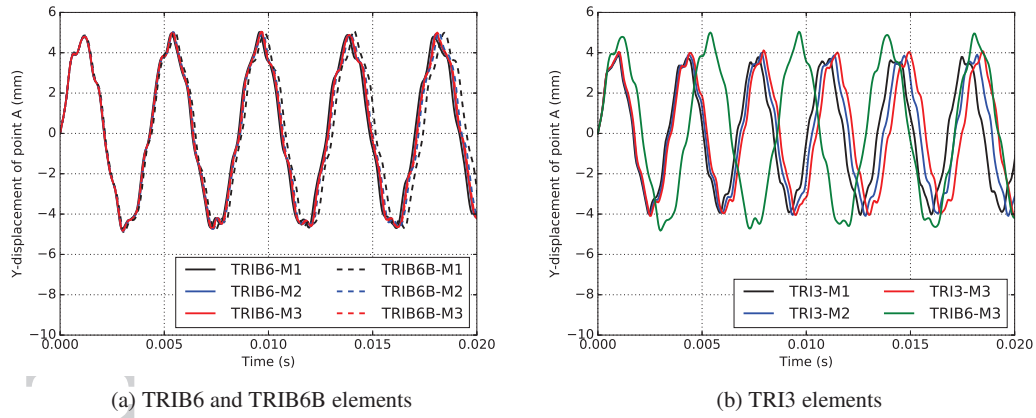


Figure 37. 2D jig: evolution of Y-displacement of point A for different meshes obtained with the implicit scheme.

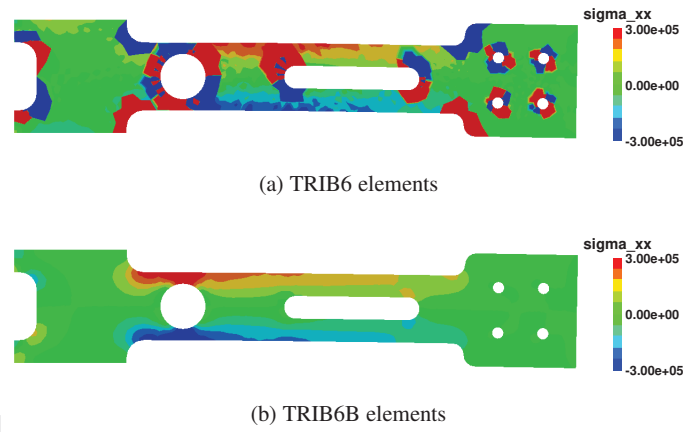


Figure 38. 2D jig: contour plots of σ_{xx} stress at $t = 0.003s$ obtained with M1 mesh.

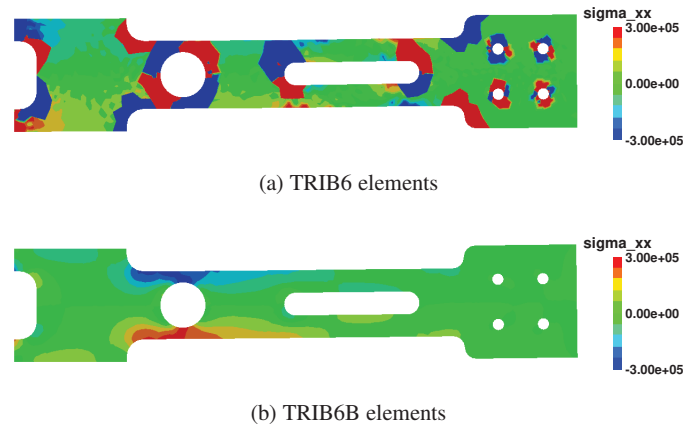


Figure 39. 2D jig: contour plots of σ_{xx} stress at $t = 0.005s$ obtained with M1 mesh.

7.4. Elastodynamics in 3D - connecting rod

As the last example, we study the elastodynamics of a model connecting rod in 3D whose geometry is as shown in Fig. 40. The Poisson's ratio of the material is assumed as 0.49999. The connecting rod is clamped on its flat faces located at $X=0$ and is excited with an initial velocity of 20 m/s in the Y-direction. The analysis is performed for two different meshes shown in Fig. 41 which consists of 4627 and 32926 elements. The total number of DOFs for the two meshes using proposed elements are 26388 and 163662, respectively.

As illustrated in Fig. 42, Y-displacement of point A obtained with the explicit scheme for both the TETB10 and TETB10B elements match well with the solution obtained with the implicit scheme; and Fig. 43 shows a clear convergence of the proposed elements as the mesh is refined. Contour plots of the bending stress (σ_{xx}) presented in Fig. 44 prove once again that the proposed scheme produces smooth stress fields. Thus, this example demonstrates the applicability of the present work to complex industrial models that can be meshed readily with the existing mesh generators.

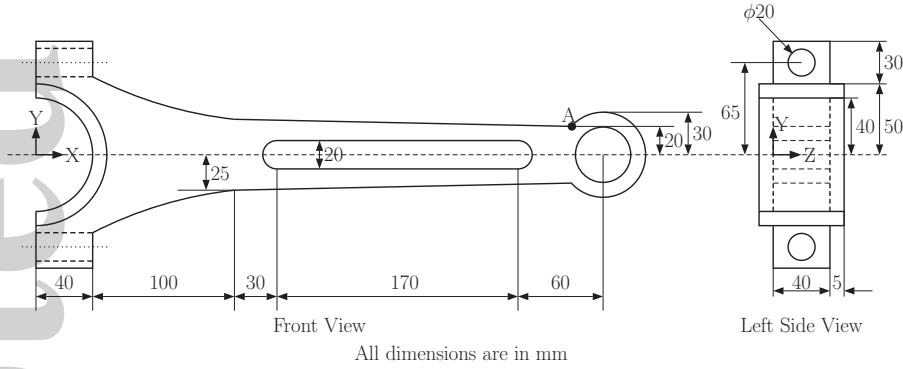


Figure 40. Connecting rod: geometry of the model. Point A is located at 40 mm in the Z direction.

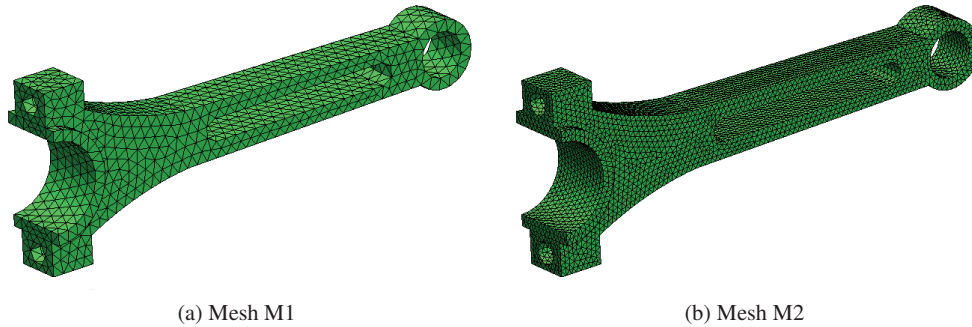


Figure 41. Connecting rod: meshes considered for the finite element analysis.

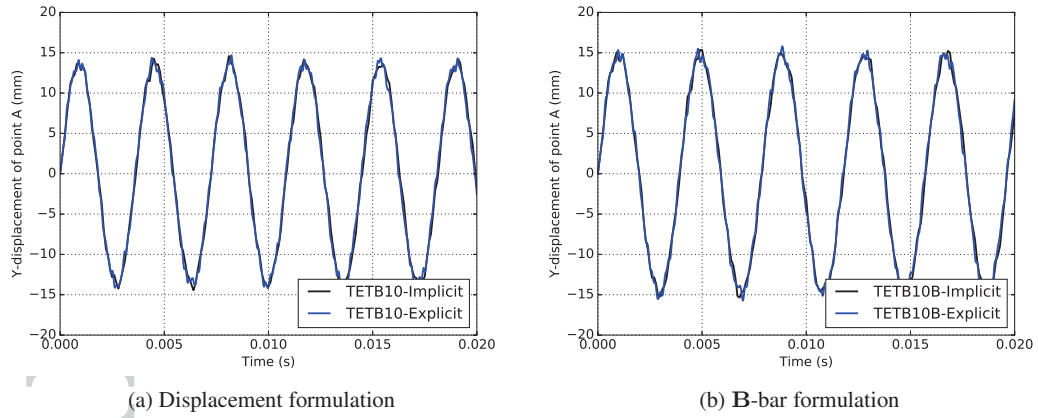


Figure 42. Connecting rod: evolution of Y-displacement of point A obtained with the mesh M1.

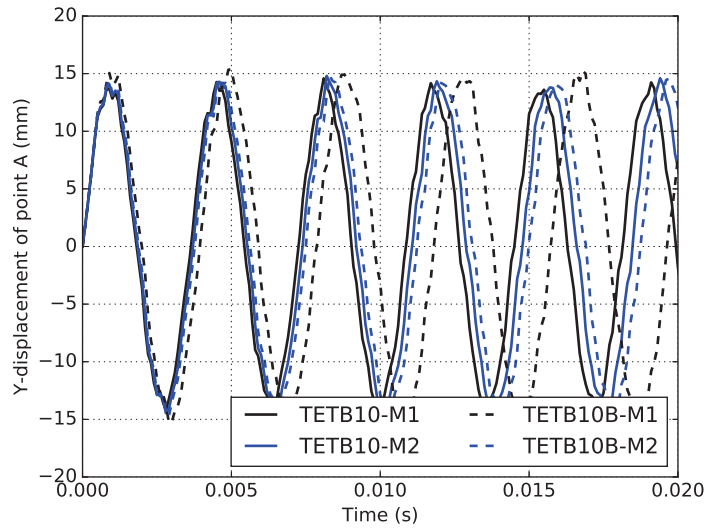


Figure 43. Connecting rod: evolution of Y-displacement of point A using the implicit scheme.

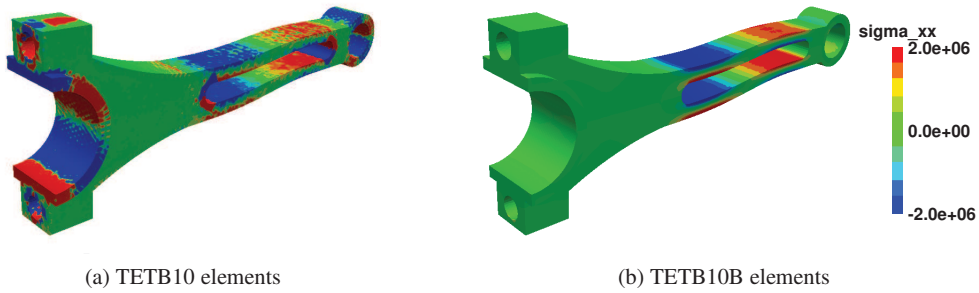


Figure 44. Connecting rod: contour plots of σ_{xx} stress obtained with the M2 mesh.

8. CONCLUSIONS

In this paper, we have presented a novel finite element scheme for performing efficient elastostatic and elastodynamic simulations involving compressible and nearly incompressible linear elastic materials using quadratic Bézier triangular and tetrahedral elements. The novel contributions of the present work are (i) Bézier elements for explicit elastodynamics, (ii) **B**-bar formulation for quadratic Bézier triangular and tetrahedral elements to deal with nearly incompressible materials, and (iii) a simple mapping technique for generating finite element meshes with quadratic Bézier elements from the quadratic Lagrange elements that can be generated using the existing mesh generators.

The inf-sup stability of the proposed **B**-bar formulation is proven by computing numerical inf-sup constants for the 2D problem of a circular annulus. By calculating error norms for the problems of a thick hollow cylinder and a thick hollow sphere subjected to internal pressure, it is proved that optimal spatial convergence rates are obtained with the proposed **B**-bar formulation irrespective of the value of Poisson's ratio ($\nu < 0.5$). The bending behaviour of the proposed elements is demonstrated using the example of Cook's membrane in 2D and a long tapered beam in 3D. The applicability of the proposed elements to elastodynamic simulations, especially explicit dynamic simulations, is demonstrated using the examples of a cantilever beam, a jig in 2D and a connecting rod in 3D.

The salient features of the present work can be summarised as:

- The proposed work employs a single finite element formulation for elastostatic as well as elastodynamic simulations.
- Accurate numerical results can be obtained with the proposed elements, even in the incompressible limit, using very coarse meshes.
- The finite element discretisations for the proposed work can be generated using existing mesh generators by making use of the simple mapping technique proposed in this work. Moreover, as the standard elimination approach is used for applying Dirichlet boundary conditions, the proposed elements can be implemented into existing finite element codes with fewer resources.
- The **B**-bar formulation proposed for dealing with nearly incompressible models does not involve any additional independent variables, nor does it increase the bandwidth of the global matrix system. Therefore, the additional cost required for the **B**-bar formulation is significantly less when compared to the mixed-stabilised methods in which additional variables are essential to deal with the issue of *locking*.
- The proposed work is completely free from mesh-size-dependent and/or material-properties-dependent parameters.
- The proposed work employs higher-order elements that distribute surface loads uniformly to all the associated control points (nodes) and that naturally render lumped-mass matrices with a homogeneous distribution of the element mass to all the nodes. These two inherent features of the Bézier elements can prove to be significant in explicit contact-impact simulations in which the standard Lagrange elements struggle.

In conclusion, the ability to use finite element meshes that can be generated using the existing mesh generators and the resulting computational benefits from using coarse meshes for obtaining

accurate numerical results, especially for explicit elastodynamic simulations with compressible as well as nearly incompressible materials, make the proposed work an accurate and cost-effective framework for performing elastodynamic simulations of complex models using fewer computational resources.

As a future work, the basic ingredients of the proposed work can be extended to other problems in the field of computational mechanics. The ongoing research effort is focused on extending the proposed elements to the problems involving nearly incompressible hyperelastic and elastoplastic material models.

ACKNOWLEDGEMENTS

The author is grateful to Prof. Djordje Perić (Swansea University), Prof. Wulf G. Dettmer (Swansea University) and Dr. Anthony Crook (Three Cliffs Geomechanical Analysis Limited) for many fruitful discussions and suggestions in improving the quality of the paper.

References

1. E. Wang, T. Nelson, and R. Rauch. Back to Elements - Tetrahedral vs. Hexahedra. *CAD-FEM GmbH, Munich, Germany*, 2004.
2. J. Bonet and A. J. Burton. A simple average nodal pressure tetrahedral element for incompressible and nearly incompressible dynamic explicit applications. *Communications in Numerical Methods in Engineering*, 14:437–449, 1998.
3. O. C. Zienkiewicz, J. Rojek, R. L. Taylor, and M. Pastor. Triangles and Tetrahedra in explicit dynamic codes for solids. *International Journal for Numerical Methods in Engineering*, 43:565–583, 1998.
4. M. Pastor, O. C. Zienkiewicz, T. Li, L. Xiaoqing, and M. Huang. Stabilized finite elements with equal order of interpolation for soil dynamics problems. *Archives of Computational Methods in Engineering*, 6:3–33, 1999.
5. C. R. Dohrmann, M. W. Heinstein, J. Jung, S. W. Key, and W. R. Witkowski. Node-based uniform strain elements for three-node triangular and four-node tetrahedral meshes. *International Journal of Numerical Methods in Engineering*, 47:1549–1568, 2000.
6. R. L. Taylor. A mixed-enhanced formulation for tetrahedral finite elements. *International Journal for Numerical Methods in Engineering*, 47:205–227, 2000.
7. Y. Guo, M. Ortiz, T. Belytschko, and E. A. Repetto. Triangular composite finite elements. *International Journal of Numerical Methods in Engineering*, 47:287–316, 2000.
8. P. Thoutireddy, J. F. Molinari, E. A. Repetto, and M. Ortiz. Tetrahedral composite finite elements. *International Journal for Numerical Methods in Engineering*, 53:1337–1351, 2002.
9. M. A. Puso and J. Solberg. A stabilized nodally integrated tetrahedral. *International Journal of Numerical Methods in Engineering*, 67:841–867, 2006.
10. G. R. Liu, K. Y. Dai, and T. T. Nguyen. A smoothed finite element method for mechanics problems. *Computational Mechanics*, 39:859–877, 2007.
11. Z. C. He, G. Y. Li, Z. H. Zhong, A. G. Cheng, G. Y. Zhang, E. Liu, G. R. Li, and Z. Zhou. An edge-based smoothed tetrahedron finite element method (ES-T-FEM) for 3D static and dynamic problems. *Computational Mechanics*, 52:221–236, 2013.
12. M. Brocardo, M. Micheloni, and P. Krysl. Assumed-deformation gradient finite elements with nodal integration for nearly incompressible large deformation analysis. *International Journal for Numerical Methods in Engineering*, 78:1113–1134, 2009.
13. E. A. de Souza Neto, F. M. Andrade Pires, and D. R. J. Owen. F-bar-based linear triangles and tetrahedra for finite strain analysis of nearly incompressible solids. Part I: formulation and benchmarking. *International Journal of Numerical Methods in Engineering*, 62:353–383, 2005.

14. P. Hansbo. A nonconforming rotated Q_1 approximation on tetrahedra. *Computer Methods in Applied Mechanics and Engineering*, 200:1311–1316, 2011.
15. P. Hansbo. Nonconforming rotated Q_1 tetrahedral element with explicit time stepping for elastodynamics. *International Journal for Numerical Methods in Engineering*, 91:1105–1114, 2012.
16. K. T. Danielson. Fifteen node tetrahedral elements for explicit methods in nonlinear solid dynamics. *Computer Methods in Applied Mechanics and Engineering*, 272:160–180, 2014.
17. A. Pakravan and P. Krysl. Mean-strain 10-node tetrahedron with energy-sampling stabilization. *International Journal for Numerical Methods in Engineering*, 109:1439–1460, 2017.
18. A. Pakravan and P. Krysl. Mean-strain 10-node tetrahedron with energy-sampling stabilization for nonlinear deformation. *International Journal for Numerical Methods in Engineering*, 111:603–623, 2017.
19. L. P. Franca, T. J. R. Hughes, A. F. D. Loula, and I. Miranda. A new family of stable elements for nearly incompressible elasticity based on a mixed Petrov-Galerkin finite element formulation. *Numerische Mathematik*, 53:123–141, 1988.
20. O. Klaas, A. Maniatty, and M. S. Shephard. A stabilized mixed finite element method for finite elasticity. Formulation for linear displacement and pressure interpolation. *Computer Methods in Applied Mechanics and Engineering*, 180:65–79, 1999.
21. A. M. Maniatty, Y. Liu, O. Klaas, and M. S. Shephard. Stabilized finite element method for viscoplastic flow: formulation and a simple progressive solution strategy. *Computer Methods in Applied Mechanics and Engineering*, 190:4609–4625, 2001.
22. A. M. Maniatty, Y. Liu, O. Klaas, and M. S. Shephard. Higher order stabilized finite element method for hyperelastic finite deformation. *Computer Methods in Applied Mechanics and Engineering*, 191:1491–1503, 2002.
23. A. Masud and K. Xia. A stabilized mixed finite element method for nearly incompressible elasticity. *Journal of Applied Mechanics*, 72:711–720, 2005.
24. K. Xia and A. Masud. A stabilized Finite element formulation for finite deformation elastoplasticity in geomechanics. *Computers and Geotechnics*, 36:396–405, 2009.
25. M. Chiumenti, Q. Valverde, C. A. de Saracibar, and M. Cervera. A stabilized formulation for incompressible elasticity using linear displacement and pressure interpolations. *Computer Methods in Applied Mechanics and Engineering*, 191:5253–5264, 2002.
26. M. Cervera, M. Chiumenti, Q. Valverde, and C. A. de Saracibar. Mixed linear/linear simplicial elements for incompressible elasticity and plasticity. *Computer Methods in Applied Mechanics and Engineering*, 192:5249–5263, 2003.
27. M. Cervera, M. Chiumenti, and R. Codina. Mixed stabilized finite element methods in nonlinear solid mechanics. Part I: formulation. *Computer Methods in Applied Mechanics and Engineering*, 199:2559–2570, 2010.
28. M. Cervera, M. Chiumenti, and R. Codina. Mixed stabilized finite element methods in nonlinear solid mechanics. Part II: strain localization. *Computer Methods in Applied Mechanics and Engineering*, 199:2571–2589, 2010.
29. M. Cervera, M. Chiumenti, L. Benedetti, and R. Codina. Mixed stabilized finite element methods in nonlinear solid mechanics. Part III: compressible and incompressible plasticity. *Computer Methods in Applied Mechanics and Engineering*, 285:752–775, 2015.
30. G. Scovazzi, B. Carnes, X. Zeng, and S. Rossi. A simple, stable, and accurate linear tetrahedral finite element for transient, nearly, and fully incompressible solid dynamics: a dynamic variational multiscale approach. *International Journal for Numerical Methods in Engineering*, 106:799–839, 2016.
31. S. Rossi, N. Abboud, and G. Scovazzi. Implicit finite incompressible elastodynamics with linear finite elements: A stabilized method in rate form. *Computer Methods in Applied Mechanics and Engineering*, 311:208–249, 2016.
32. X. Zeng, G. Scovazzi, N. Abboud, O. Colomés, and S. Rossi. A dynamic variational multiscale method for viscoelasticity using linear tetrahedral elements. *International Journal for Numerical Methods in Engineering*, 112:1951–2003, 2017.
33. G. Scovazzi, T. Song, and X. Zeng. A velocity/stress mixed stabilized nodal finite element for elastodynamics: Analysis and computations with strongly and weakly enforced boundary conditions. *Computer Methods in Applied Mechanics and Engineering*, 325:532–576, 2017.
34. C. H. Lee, A. J. Gil, and J. Bonet. Development of a cell centred upwind finite volume algorithm for a new conservation law formulation in structural dynamics. *Computers and Structures*, 118:13–38, 2013.
35. C. H. Lee, A. J. Gil, and J. Bonet. Development of a stabilised Petrov-Galerkin formulation for conservation laws in Lagrangian fast solid dynamics. *Computer Methods in Applied Mechanics and Engineering*, 268:40–64, 2014.
36. A. J. Gil, C. H. Lee, J. Bonet, and M. Aguirre. A stabilised Petrov-Galerkin formulation for linear tetrahedral elements in compressible, nearly incompressible and truly incompressible fast dynamics. *Computer Methods in Applied Mechanics and Engineering*, 276:659–690, 2014.

37. J. Bonet, A. J. Gil, C. H. Lee, M. Aguirre, and R. Ortigosa. A first order hyperbolic framework for large strain computational solid dynamics. Part I: total Lagrangian isothermal elasticity. *Computer Methods in Applied Mechanics and Engineering*, 283:689–732, 2015.
38. J. A. Cottrell, Y. Bazilevs, and T. J. R. Hughes. *Isogeometric analysis: toward integration of CAD and FEA*. John Wiley & Sons, Chichester, England, 2009.
39. F. Auricchio, L. Beirão de Veiga, T. J. R. Hughes, A. Reali, and G. Sangalli. Isogeometric collocation for elastostatics and explicit dynamics. Technical report, The Institute for Computational Engineering and Sciences, The University of Texas at Austin, 2012.
40. L. Chen, N. Nguyen-Thanh, H. Nguyen-Xuan, T. Rabczuk, S. P. A. Bordas, and G. Limbert. Explicit finite deformation analysis of isogeometric membranes. *Computer Methods in Applied Mechanics and Engineering*, 277:104–130, 2014.
41. N. Jaxon and X. Qian. Isogeometric analysis on triangulations. *Computer-Aided Design*, 46:45–57, 2014.
42. S. Xia and X. Qian. Isogeometric analysis with Bézier tetrahedra. *Computer Methods in Applied Mechanics and Engineering*, 316:782–816, 2017.
43. C. Kanduč, T. Giannelli, F. Pelosi, and H. Speleers. Adaptive isogeometric analysis with hierarchical box splines. *Computer Methods in Applied Mechanics and Engineering*, 316:817–838, 2017.
44. L. Engvall and J. A. Evans. Isogeometric triangular Bernstein-Bézier discretizations: Automatic mesh generation and geometrically exact finite element analysis. *Computer Methods in Applied Mechanics and Engineering*, 304:378–407, 2016.
45. L. Engvall and J. A. Evans. Isogeometric unstructured tetrahedral and mixed-element Bernstein-Bézier discretizations. *Computer Methods in Applied Mechanics and Engineering*, 319:83–123, 2017.
46. S. P. Oberrecht, J. Novák and P. Krysl. B-bar FEMs for anisotropic elasticity. *International Journal for Numerical Methods in Engineering*, 98:92–104, 2014.
47. L. Piegl and W. Tiller. *The NURBS Book (Monographs in Visual Communication)*. Springer-Verlag, New York, 1997.
48. J. A. Nitsche. Über ein Variationsprinzip zur Lösung von Dirichlet-Problemen bei Verwendung von Teilräumen, die keinen Randbedingungen unterworfen sind. *Abhandlungen aus dem Mathematischen Seminar der Universität Hamburg*, 36:9–15, 1970-1971.
49. W. G. Dettmer, C. Kadapa, and D. Perić. A stabilised immersed boundary method on hierarchical b-spline grids. *Computer Methods in Applied Mechanics and Engineering*, 311:415–437, 2016.
50. C. Kadapa, W. G. Dettmer, and D. Perić. A stabilised immersed boundary method on hierarchical b-spline grids for fluid-rigid body interaction with solid-solid contact. *Computer Methods in Applied Mechanics and Engineering*, 318:242–269, 2017.
51. C. Kadapa, W. G. Dettmer, and D. Perić. A stabilised immersed framework on hierarchical b-spline grids for fluid-flexible structure interaction with solid-solid contact. *Computer Methods in Applied Mechanics and Engineering*, 335:472–489, 2018.
52. O. C. Zienkiewicz and R. L. Taylor. *The Finite Element Method. Volume 1: The Basics*. Elsevier Butterworth and Heinemann, Oxford, England, Fifth edition, 2000.
53. T. J. R. Hughes. *The Finite Element Method: Linear Static and Dynamic Finite Element Analysis*. Dover Publications, 2000.
54. K. J. Bathe. *Finite Element Procedures*. Prentice Hall Inc., New Jersey, 1996.
55. C. Kadapa. *Mixed Galerkin and least-squares formulations for isogeometric analysis*. PhD thesis, College of Engineering, Swansea University, 2014.
56. C. Kadapa, W. G. Dettmer, and D. Perić. Subdivision based mixed methods for isogeometric analysis of linear and nonlinear nearly incompressible materials. *Computer Methods in Applied Mechanics and Engineering*, 305:241–270, 2016.
57. T. J. R. Hughes. Generalization of Selective Integration Procedures to Anisotropic and Nonlinear Media. *International Journal for Numerical Methods in Engineering*, 15:1413–1418, 1980.
58. I. C. Nagtegaal, D. M. Parks, and J. R. Rice. On numerically accurate finite element solutions in the plastic range. *Computer Methods in Applied Mechanics and Engineering*, 4:153–177, 1974.
59. J. Chung and J. M. Lee. A new family of explicit time integration methods for linear and non-linear structural dynamics. *International Journal for Numerical Methods in Engineering*, 37:3961–3976, 1994.
60. C. Kadapa, W. G. Dettmer, and D. Perić. On the advantages of using the first-order generalised-alpha scheme for structural dynamic problems. *Computers and Structures*, 193:226–238, 2017.
61. Hypermesh (<https://altairhyperworks.com/product/hypermesh>).
62. D. Chapelle and K. J. Bathe. The inf-sup test. *Computers and Structures*, 47:537–545, 1993.